

Struktur- und Lumineszenzuntersuchungen an unterschiedlich präparierten, modifizierten und strukturierten nanoporösen Si-Schichten

Dissertation
zur Erlangung des akademischen Grades
doktor rerum naturalium
(Dr. rer. nat.)

vorgelegt
der Fakultät für Naturwissenschaften
der Technischen Universität Chemnitz-Zwickau

von Diplomphysikerin Anna Bruska
geboren am 08.08.1969 in Toruń

Chemnitz, den 19.09.1996

Bibliographische Beschreibung

Bruska, Anna

Struktur- und Lumineszenzuntersuchungen an unterschiedlich präparierten, modifizierten und strukturierten nanoporösen Si-Schichten

Dissertation A

Technische Universität Chemnitz-Zwickau,
Institut für Physik,
Chemnitz, 1995

163 Seiten, 68 Bilder, 4 Tabellen, 256 Literaturstellen, 14 Thesen

Referat : Die vorliegende Arbeit beschreibt die Herstellung, Strukturierung und Modifizierung von porösem Silizium. Es wird der Mechanismus der Lumineszenz in porösem Silizium und der Einfluß von Herstellungsparametern und einer Dotierung mit Laserfarbstoffen auf die optischen Eigenschaften von porösem Silizium untersucht. Für die optische Charakterisierung wurden Photolumineszenz-, Photolumineszenzanregungs- und Kathodolumineszenzspektren aufgenommen. Weiterhin werden Methoden zur Erzeugung von porösen Mikrostrukturen mit Hilfe eines ECSTM sowie zum Schreiben von optischen Mustern in porösem Silizium durch einen Elektronenstrahl vorgestellt. Strukturelle Untersuchungen wurden mit einem SEM und einem TEM durchgeführt.

Schlagwörter : Silicium, Optische Eigenschaft, Photolumineszenz, Kathodolumineszenz, Mikrostruktur, Muster, Ätzen, Elektronenmikroskopie, Lumineszenz, Siliciumoxide, Rastersondenmikroskopie, Farbstoff

Contents

List of Figures	12
List of Tables	13
List of Symbols	15
Einleitung	15
1 Porous Silicon	18
1.1 Formation of porous silicon	18
1.2 Porous silicon formation models	22
1.3 Structure of porous silicon	24
1.4 Luminescence	28
1.4.1 Photoluminescence	28
1.4.2 Electroluminescence	31
1.4.3 Cathodoluminescence	32
1.5 Luminescence mechanism models	33
1.5.1 Quantum Confinement	34
1.5.2 Specific compounds at inner surfaces	36
1.5.3 Amorphous structure: $a - Si : H$, $a - SiO_x : H$	37
1.5.4 Surface states	39
2 Experimental data	41
2.1 Preparation of porous silicon layers	41

2.2	Measurements of optical properties	42
2.2.1	Photoluminescence and Excitation	42
2.2.2	Time-Resolved Spectroscopy	43
2.3	Structural measurements	44
2.3.1	Scanning Electron Microscopy	44
2.3.2	Cathodoluminescence Mapping	46
2.3.3	Transmission Electron Microscopy	47
2.3.4	Scanning Tunneling Microscopy	49
2.3.5	Scanning Electrochemical Tunneling Microscopy	51
3	Free Standing PS Films	54
3.1	Description of samples	55
3.2	Results and Discussion	56
4	Structure and Luminescence	65
4.1	Sample preparation	67
4.2	Variation of HF concentration	67
4.2.1	Structure analysis	67
4.2.2	Spectroscopic measurements	69
4.3	Variation of current density	70
4.3.1	Structure analysis	70
4.3.2	Spectroscopic measurements	71
4.4	Variation of Pt layer	77
4.5	Gauss Deconvolution	79
4.6	Discussion and Summary	84
5	Porous Silicon doped with Dyes	87
5.1	Description of samples	88
5.1.1	Rhodamine 110	88
5.1.2	Kiton Red and Stilbene1	88
5.1.3	Coumarine 153	90

5.2	Results and Discussion	91
5.2.1	Rhodamine 110	91
5.2.2	Kiton Red and Stilbene1	97
5.2.3	Coumarine 153	100
5.3	Summary	107
6	"Writing" of Optical Patterns	109
6.1	Description of samples and instrumentations	110
6.2	Results and Discussion	111
6.2.1	Structure and Luminescence	111
6.2.2	Fabrication of optical patterns	114
6.3	Summary	119
7	Microstructures of PS	120
7.1	Experimental Data	121
7.1.1	Devolopment of ECSTM	121
7.1.2	Description and characterization of samples	127
7.2	Fabrication of microstructures by ECSTM	128
7.2.1	Structure Analysis	128
7.2.2	Cathodoluminescence	131
7.3	Summary	132
	Zusammenfassung	133
	Bibliography	137
	Selbständigkeitserklärung	157
	Thesen	159
	Danksagung	163

List of Figures

1.1	Typical anodic I-V characteristics for silicon in HF for different dissolution regions. In a region A, pore formation occurs, and in a region C, electropolishing process is observed. Region B is a transition zone between the pore formation and electropolishing. Scale units and zeros are arbitrarily chosen and depend on silicon sample and experimental conditions [10]. J_{ps} corresponds to a critical value of the current density for the pore formation.	19
1.2	Schematic description of Beale model (a) and of a quantum model (b). Figure b (bottom part) shows the corresponding band diagram of the interface above and the two corresponding different energy barriers for a hole penetration into a wall (broken arrow) or a pore tip (solid arrow)	23
1.3	Cross-sectional TEM micrographs showing the basic differences in the morphology between p, n, p^+ , and n^+ . (a) p-type silicon. Pore diameters are extremely small and highly interconnected. (b) n-type silicon. Strong tendency to form straight channels. (c) p^+ -type silicon. Tendency to form small 5-10 nm channels with numerous side branches. (d) n^+ -type silicon. Virtually identical to p-type silicon. The current direction for all samples is from bottom to top and the anodization conditions are 49 % HF at 10 mA/cm^{-2} [25].	26

1.4	Influence of UV light on the photoluminescence of as-prepared sample (our own measurements).	30
1.5	The idealized structure of annealed siloxene $Si_6O_3H_6$	36
1.6	Tuning of colour of luminescence via chemical substitution of halogen and OH groups [106]	38
1.7	Configurational coordinate diagram and possible photoluminescence process in porous Si. Bands for an electron-hole pair in a Si nanostructure and bulk Si, an excited state of a luminescence center and a ground state are shown as a function of the configurational coordinate, q , related to the local lattice distortion around the luminescence center [113].	39
2.1	Schematic presentation of the anodization cell for the PS formation.	42
2.2	Experimental set-up for measurements of time-resolved spectroscopy.	43
2.3	The schematic view of the SEM system	45
2.4	The schematic diagram of the CL experimental system	46
2.5	The schematic view of the TEM system	48
2.6	The schematic diagram of the STM.	50
2.7	Scanning tunneling microscopes can be operated in either the constant current mode (left side) or the constant height mode (right side) [129].	51
2.8	Schematic presentation of SECM. The tunneling voltage U_T is defined by the difference of E_T and E_S . I/V=current/voltage converter for measuring I_T . Potentiostat P controls independently E_T and E_S [131]	52
3.1	Light microscopic (a) and SEM (b) image of free-standing PS sample.	57

3.2	Cross section SEM images of the angle at the edge of the film (a, b, c) and of a side of the edge (d) pictures correspond to different magnifications, as indicated in the figures	58
3.3	Transmission electron bright (a) and dark field (b) images . .	59
3.4	High resolution transmission electron micrograph (a) and a related diffraction pattern (b) of a free-standing PS film in plan view, lattice fringes correspond to Si [220] planes with a spacing of 1.92 Å. The diffraction pattern is related to the $\langle 111 \rangle$ direction oriented parallel to the electron beam.	60
3.5	Transmission electron bright field (a) image and a related diffraction pattern (b) of free-standing PS film in cross sectional view. The diffraction pattern is related to the $\langle 110 \rangle$ direction oriented parallel to the electron beam.	61
3.6	The cross-sectional SEM image of free standing PS films prepared at a current density of $60 \text{ mA} \cdot \text{cm}^{-2}$ for 35 min and finally etched at a current density of $120 \text{ mA} \cdot \text{cm}^{-2}$. Each layer is $\sim 20 \mu\text{m}$ thick	62
3.7	Cross sectional SEM image of the PS sample prepared with a current density of $127.5 \text{ mA} \cdot \text{cm}^{-2}$ ((100) p-type silicon substrate (boron-doped), a resistivity of $10 \Omega \cdot \text{cm}$ and a solution of HF (40% wt)+ $\text{C}_2\text{H}_5\text{OH}$ (1:1), t_A 20 s).	63
4.1	Cross-sectional SEM images of porous silicon layers for two HF concentration (a) 10% and (b) 40%	68
4.2	The room-temperature photoluminescence spectra of porous Si observed with excitation light of 366 nm for the samples 1a, 1b, 1c, 1d prepared with 10%, 20%, 30% and 40% HF, respectively. The maxima appear to be skewed towards higher energy with decreasing HF concentrations.	69

4.3	A cross-sectional SEM image of porous silicon layer of sample 2a	71
4.4	STM top view of porous silicon layer of sample 2a and 2d . . .	72
4.5	Cross-sectional (a, b) and top view SEM (c, d) images of porous silicon samples prepared for two different current density: at $127.5 \text{ mA} \cdot \text{cm}^{-2}$ (a, c) and $25.5 \text{ mA} \cdot \text{cm}^{-2}$ (b, d) . . .	72
4.6	Luminescence spectra of porous Si observed with excitation radiation of 254 nm for PS samples prepared with different current density (a) 25.5, (b) 51, (c) 76.5, (d)102, (e) 127.5 $\text{mA} \cdot \text{cm}^{-2}$ at room temperature.	73
4.7	Luminescence spectra of porous Si observed at two different excitation radiation of 254 nm and 436 nm for PS sample 2c prepared with a current density of $76.5 \text{ mA} \cdot \text{cm}^{-2}$	74
4.8	PLE spectra of porous Si observed for two different emission bands of 620 nm and 660 nm for PS sample prepared with a current density of $76.6 \text{ mA} \cdot \text{cm}^{-2}$	76
4.9	Normalized PL spectra of porous Si observed with excitation light of 254 nm for the sample 2a and the sample 2d with (b, d) or without a Pt film (a, c), respectively	77
4.10	Deconvolution of PL spectrum into two Gaussians of sample 2e measured with excitation radiation of 436 nm.	81
4.11	Comparison of experimental data with fitting (four Gaussians) for PL spectra of sample 2c observed at excitation radiation of 254 nm and of 436 nm. Dotted curve designates the experimental data (upper part). Standart deviation of fitting to experimental data measured at 254 nm (dotted line) and at 436 nm (solid line) (lower part)	83
5.1	The chemical structure of Rhodamine 110	88

5.2	The chemical structure of Stilbene 1 (St1)	89
5.3	The chemical structure of Kiton Red 620 (Kt)	89
5.4	Idealized cross-sectional schematic view showing dye impreg- nation in PS samples (a) when freshly etched (b) when aged. .	90
5.5	The chemical structure of Coumarine 153	91
5.6	Cross-sectional SEM micrographs of the PS samples, (sample A and sample B)	92
5.7	The schematic description of porous structure. Interface 1 (1) between the crystallite C and layer L and the interface 2 (2) between the layer L and air.	92
5.8	The room temperature normalized photoluminescence spectra of porous silicon measured with excitation at 250 nm.	93
5.9	PL spectra (normalized for intensity of red band) of sample A before and after doping with laser dyes Rh110 measured with an excitation wavelength of 436 nm.	94
5.10	Normalized PL spectra (normalized for intensity of red band) of sample B before and after doping with laser dyes Rh110 measured with an excitation wavelength of 436 nm	95
5.11	SEM images of the PS layers impregnated with Stilbene 1 using two different techniques mentioned in the chapter 6.1.2. .	98
5.12	Normalized PL spectra of the samples doped with laser dyes (sample 1C, 2C with Stilbene 1 and sample 1D, 2D with Kiton Red)	99
5.13	Normalized PL spectra (normalized for intensity of the band at 2.0 eV) of sample 1E before (solid line) and after doping (dotted line) with the laser dye Cou153 measured at an exci- tation wavelength of 254 nm	101
5.14	Normalized PLE spectra of sample 1E measured at an emission wavelength of 720 nm and of 665 nm	102

5.15	Normalized PLE spectra of sample E after doping with Cou153 measured at an emission wavelength of 530 nm (upper part) and the absorption spectrum of Coumarine 153 dissolved in ethanol (lower part)	103
5.16	Normalized PL spectra (normalized for intensity of the red band) of sample 1E before and after doping with the laser dye Cou153 measured at an excitation wavelength of 436 nm . . .	104
5.17	Normalized PLE spectra of sample E before and after doping with the laser dye Cou153 measured at emission wavelength of 665 nm	105
5.18	Fluorescence decay of Coumarine 153 in PS sample :experimental data (dotted line) and fit (solid line) measured at 530 nm	106
6.1	SEM images of the surface morphology of a PS sample. We can see the difference in the roughness of the PS layers (a) structure 1 and (b) structure 2 of the sample B.	111
6.2	Cross-sectional SEM image of the porous sample	112
6.3	PL spectra of the same porous Si sample observed with two different excitation wavelengths of 254 nm and of 300 nm . . .	113
6.4	The cathodoluminescence spectra of a structure 1 (dashed line) and 2 (solid line) of the PS sample	114
6.5	The cathodoluminescence (a, b, c) and surface topography (d) of the porous sample. The written dark pattern is pointed by the arrows.	115
6.6	Cathodoluminescence image of a fabricated pattern : TU Chemnitz	116
6.7	The light microscopic image of the pattern. The bright regions shows the red luminescence.	116

6.8	SEM image of the region irradiated with an electron beam. . .	117
7.1	Schematic description of a fabrication of PS microstructure of using modifying STM-like device.	121
7.2	The STM-like device (ECSTM) set-up based on Hansma's STM (upper part) and an anodization cell (lower part)	122
7.3	Fabrication procedure of PS microstructure	124
7.4	SEM image of an etched Pt tip	125
7.5	SEM image of a wax-coated Pt tip	126
7.6	SEM images of PS microstructures (sample A) low magnifi- cation (a), a single etch-patch (b) and (c) porous structure within a single etch-patch from (b)	129
7.7	SEM image of an etch-patch of 2 μm (sample B)	130
7.8	SEM image of an insulated Pt tip after etching	131
7.9	SEM (a) and cathodoluminescence (b) images of an etch-patch	132

List of Tables

4.1	The position of each peak for the deconvolution into two, three, four Gaussians of PL spectra.	80
4.2	The ratio of the relative intensities of two Gaussians at ≈ 2.05 eV and at ≈ 1.87 eV for different J_A	82
4.3	The FWHM and the area of single Gauss band for different current densities	84
7.1	Anodization parameters of samples A, B and C	127

List of Symbols

PS	Porous Silicon
PL	Photoluminescence
PLE	Photoexcitation
CL	Cathodoluminescence
TRS	Time-Resolved Spectroscopy
TRF	Time-Resolved Fluorescence
HF	Hydrofluoric Acid
SEM	Scanning Electron Microscopy
TEM	Transmission Electron Microscopy
STM	Scanning Tunneling Microscopy
ECSTM	Electrochemical Scanning Tunneling Microscopy

Einleitung

Kristallines Silicium ist heutzutage die Grundlage der modernen Computer- und Telekommunikationsindustrie und aus diesem Grund auch eines der am besten untersuchten Materialien. Durch seine physikalischen und chemischen Eigenschaften ist Silicium nahezu unersetzlich für die Herstellung von Prozessor- und Speicherchips und kann in absehbarer Zeit durch kein anderes Material abgelöst werden.

In den letzten Jahren ist man bei der Entwicklung neuer, schnellerer und effektiverer Halbleiter auf immer neue Probleme gestoßen. Quanteneffekte, die die Funktion der konventionellen Bauelemente stören, machen eine weitere Miniaturisierung in naher Zukunft unmöglich. Deshalb sind Wissenschaftler auf der ganzen Welt auf der Suche nach neuen Technologien um den Integrationsgrad von Halbleiterbauelementen zu erhöhen. Dies führt zur Zeit zu einer dynamischen Entwicklung des Gebietes der Optoelektronik, in dem nicht ein elektrischer Strom, sondern Licht zur Informationsübertragung dient. Dieses Gebiet dominieren zur Zeit noch teure und technologisch aufwendig herzustellende III-V Halbleiter. Silicium emittiert aufgrund seiner relativ kleinen und indirekten Bandlücke nur sehr schwach infrarotes Licht. Obwohl dieses Problem in anderen indirekten Halbleitermaterialien durch die Nutzung von kurzreichweitigen "Central Cell" Potentialen isoelektrischer Verunreinigungen, die den k-Raum "aufweichen", umgangen werden konnte, ist eine derartige thermisch stabile Verunreinigung im Silicium noch

unbekannt [90]. Die gezielte Veränderung der Bandlücke unter Benutzung von Si/SiGe Systemen erwies sich zwar als erfolgreich, jedoch auch als sehr kompliziert in der Herstellung. Aus diesen Gründen ist die Begeisterung, die aus der Entdeckung der eher starken sichtbaren Lumineszenz von sogenanntem "porösem Silicium" durch Canham entstand, verständlich. Die Photonenenergie dieser Lumineszenz liegt weit über einem Elektronenvolt und ist wesentlich intensiver als die des Silicium-Substrates. Damit könnten auch auf Silicium basierende optoelektronische Bausteine Anwendung in VLSI-Schaltkreisen, Lasern oder bei der Herstellung von Flachbildschirmen finden. Für eine optoelektronische Anwendung ist es sehr wichtig die Lumineszenzprozesse zu verstehen, sie zu kontrollieren und dadurch auch verbessern zu können. Bisher sind die Lumineszenzmechanismen noch ungeklärt. Es wurden einige physikalische Modelle wie z.B. ein Quantum-Confinement in dünnen Quantendrähten und/oder Kristalliten [1], die Lumineszenz von SiH_x [60], [83], amorphem Silicium bzw. von Oberflächenzuständen [112] vorgeschlagen. Neuere Ergebnisse erklären die Lumineszenz auch durch ein Quantum Confinement/Lumineszenzzentren (QCLC) Modell [137]. Dabei findet die elektronische Anregung in Siliciumnanostrukturen statt, gefolgt von einem Tunnelprozeß der Ladungsträger und der Rekombination in der SiO_x Schicht an der Oberfläche [138], [137], [42], [139],[99], [140], [141], [72], [142]. Ein wichtiger Aspekt dieses Modells ist, daß das Emissionsspektrum des porösen Siliciums durch Lumineszenzzentren geprägt wird. In diesem Fall sollte man erwarten, daß die Emmission sich als eine Überlagerung von mehreren Banden, wie bei kristallinem und amorphen SiO_2 ($a-SiO_2$) beobachtet, darstellt [143], [144]. Jedoch existieren bisher noch nicht genügend Belege für die Richtigkeit dieses Modells.

In Kapitel 2 werden die theoretischen Grundlagen, insbesondere die Lumineszenzeigenschaften, der Bildungsprozeß und die Struktur des PS erläutert. Meine Untersuchungen zum Verständnis der Lumineszenzmechanismen des

PS werde ich im Kapitel 5 schildern. Dabei unterstützen meine Ergebnisse das QCLC Modell von Qin and Jia [137], und es wird auch auf die Lumineszenz durch Störstellen in der Oberfläche und im SiO_x tieferliegenden Lumineszenzzentren eingegangen. Kapitel 4 beschäftigt sich mit strukturellen Untersuchungen an freistehenden PS-Schichten, die mit Hilfe von SEM, TEM und optischer Mikroskopie durchgeführt wurden. Die experimentellen Grundlagen dazu enthält Kapitel 3. Dort werden die Mechanismen die zur Schichtstruktur in freistehendem PS führen erläutert.

Kapitel 6 beschreibt die experimentellen Ergebnisse der Messungen an mit Laserfarbstoffen (Coumarine 153, Stilbene 1, Kiton Red, Rhodamine 110) dotierten PS-Proben. Der Schwerpunkt der Untersuchungen liegt hier auf der Modifizierung der Lumineszenz durch eine Dotierung mit Farbstoffen.

Kapitel 7 ist der Erzeugung von optischen Mustern im Mikrometerbereich in PS durch einen als lithographisches Werkzeug verwendeten Elektronenstrahl gewidmet. Weiterhin werden Kathodolumineszenzmessungen bei Raumtemperatur und bei 77 K vorgestellt.

Abschließend berichte ich im Kapitel 8 über die Herstellung von porösen Mikrostrukturen an auf Silicium durch ein elektrochemisches STM-ähnliches Gerät. Die Struktur- und Lumineszenzeigenschaften dieser Objekte wurden mit Hilfe von SEM und Kathodolumineszenzmessungen untersucht.

Chapter 1

Porous Silicon

It could be believed, that the different environmental conditions that have an effect on the PS properties can be viewed as a disadvantage. If their influence is, however, understood, they give possibility not only of studying the physics and chemistry of PS formation but also of controlling its properties [5].

In this chapter, the already known structural as well as optical properties of porous silicon will be shown.

1.1 Formation of porous silicon

Over the past 30 years, porous Si samples have been fabricated by a variety of techniques, including those of stain etching [2], spark erosion [3] and related techniques [4]. However by far the most common method is that of electrochemical anodization in a HF solution. Nevertheless, despite extensive study of the corresponding electrochemistry of pore formation, its underlying mechanism is not well understood. It is generally accepted that holes as carriers are required in the initial oxidation steps, in order to release hydrogen to facilitate etching and oxidation [5] and that this is the reason why additional light irradiation is necessary for n-type substrates. To date, understanding

of porous silicon formation stems from observations of the I-V relationships and inferences from elementary silicon electrochemistry [6], [7], [8]. For n- and p-type silicon in aqueous HF, the "typical" I-V curves show some basic similarities to the normal Schottky diode behaviour expected from semiconductor/electrolyte interfaces, including photogenerated currents at reverse bias. There are, however, some important anomalies [9], [6], [7]. The behaviour of the silicon wafer has been observed to be dependent on the sign of the applied potential and the type of material. Under cathodic polarizations

Figure 1.1: Typical anodic I-V characteristics for silicon in HF for different dissolution regions. In a region A, pore formation occurs, and in a region C, electropolishing process is observed. Region B is a transition zone between the pore formation and electropolishing. Scale units and zeros are arbitrarily chosen and depend on silicon sample and experimental conditions [10]. J_{ps} corresponds to a critical value of the current density for the pore formation.

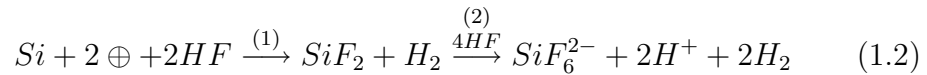
for both n- and p-type materials, the formation of porous silicon does not take place. The evolution of hydrogen gas is, however, observed. Only un-

der anodic polarizations does silicon dissolution occur and here the reaction depends strongly on the magnitude of the anodic etching.

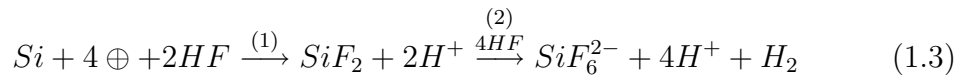
Fig. 1.1 shows the "typical" I-V curve of p-type in dark and n-type illuminated during the anodic dissolution for the different dissolution regions labeled A-C. In region A, the pore formation occurs. This is the case for current densities below a critical value of J_{ps} (Fig. 1.1). J_{ps} is a function of temperature (T) and HF concentration (c) [11]:

$$J_{ps} = A \cdot \exp\left(\frac{-E_a}{kT}\right) \cdot c^{\frac{3}{2}} \quad (1.1)$$

in which J_{ps} is in A/cm^2 , $E_a=0.345$ eV, $k=8.6171 \cdot 10^{-5}$ eV/K, c in wt. % HF, T in K and $A=3300 \cdot (wt.\%HF)^{-\frac{3}{2}} A/cm^2$. For current densities larger than J_{ps} electropolishing is observed (region C). In the transition region B, both pore formation and electropolishing processes co-exist. The corresponding resulting structure here is generally porous, but the pore diameters increase rapidly as the electropolishing regime (region C) is approached. During pore formation in region A of the Fig. 1.1, hydrogen gas evolves in a 2:1 atomic ratio to silicon. This ratio is diminished in the transition region and disappears in the electropolishing region. By measuring the current efficiencies it was estimated that approximately two electrons per dissolved silicon atom are generated during the pore formation (Eq. 1.2) and approximately four electrons (Eq. 1.3) in the electropolishing regime [12], [13].



or



Whereas the reaction (1) is electrochemical, the reaction (2) is a chemical process (Eq. 1.2 and Eq. 1.3). The stable end product of this process is H_2SiF_6 . This is independent of whether pore formation or electropolishing

occur or not. Mechanistically, this means that two or four holes participate in pore formation and electropolishing, respectively. However the exact nature of the reactions is still in dispute and several different mechanistic variants exist in order to explain the transition from a divalent to tetravalent oxidation mechanism [5].

An alternative technique for the formation of visible light emitting Si is stain-etching. In this method the samples are produced by an immersion of Si wafers in stain etches consisting of HF/HNO_3 , $HF/NaNO_2$ or HF/CrO_3 . The fabrication process, which requires no special equipment, is much easier than that of anodic etching. This suggests that it could be a technologically useful alternative approach for luminescent PS fabrication. However, recent studies [14] have indicated that stain etched PS is predominantly amorphous, thus questioning its potential usefulness as a preparation technique.

Visible light emitting Si can be made not only from anodization but also from surface damaging. Such techniques have the strong advantage of producing uniformed and patterned materials [15]. One such method is that of dry spark-erosion using high frequency (kHz range), high voltage (several thousand volts) and low current (several mA) electric sparks between a silicon substrate and a counter electrode [16]. This can be used in the preparation of p-type as well as n-type PS.

An alternative preparation method is combination of plasma chemical vapor deposition of the silicon films in a low-pressure glow discharge containing silane and hydrogen together with post-oxidation and annealing in forming gas. The deposition can be either in silane diluted with hydrogen or by chemical transport of silicon in a hydrogen plasma. The latter technique provides a better control of the crystallite size within 100 Å to 25-30 Å [17]. The PL peak position is independent of the crystallite size.

1.2 Porous silicon formation models

Presently, there are three distinct models, which have been independently proposed to account for pore formation in porous silicon: the Beale model, the diffusion-limited model and a quantum model.

The Beale model

The Beale model [18] is based on simple electrostatic arguments. The geometry of the pores generates concentrations of electric field at the pore tips, which attract carriers to these regions. These carriers are then free to contribute to chemical reactions forming further PS layers. This "positive feedback" mechanism is prevented from "running away" by the formation of a depletion region [19] in the PS hindering further movement of charge to the pore tips (Fig. 1.2a).

The diffusion-limited model

The diffusion-limited model, proposed by Smith et al.[20], describes the formation of porous silicon in terms of a stochastic random walk. It explains pore generation as resulting from the diffusion of an electroactive species such as holes to the silicon surface. The randomness is introduced by assuming that the pore tips are the most likely contact sites for a particle [20]. In addition, the selective dissolution at surface irregularities is introduced in the model predicted by Beale et al. [18]. The morphology of the porous silicon layer is characterized by the diffusion length, which is a function of the dopants concentration, voltage etc. It provides a simple understanding of pore formation in terms of basic semiconductor electrochemistry.

The quantum model

The quantum model, proposed by Canham [1], Lehmann and Gösele [21], and Foll [9] explains the pore formation in terms of increasing band gaps due to quantum charge confinement within the small dimensions of the silicon

Figure 1.2: Schematic description of Beale model (a) and of a quantum model (b). Figure b (bottom part) shows the corresponding band diagram of the interface above and the two corresponding different energy barriers for a hole penetration into a wall (broken arrow) or a pore tip (solid arrow)

”wires” formed in porous silicon. Fig. 1.2 b shows the sketch of the PS-silicon substrate interface and the corresponding band diagram. If a hole h^{\oplus} in the bulk silicon approaches the interface to the PS it needs additional energy E_{ad} to penetrate into a wall between two pores (broken arrows), whereas no additional energy is necessary to move to a pore tip (solid arrows). As a result, the pore walls will be depleted of holes (h^{\oplus}) and therefore will

become electrochemically inert, whereas the dissolution reaction continues at the pore tips. This process is self-adjusting: the increased band gap decreases the concentration of mobile charges within the remaining silicon structure and creates a "depletion region" similar in function to the depletion layer of the Beale model. The process of thinning of the walls will continue until the band gap increases to a point where the energy barrier for the hole h^{\oplus} diffusion becomes prohibitively large. The wall becomes depleted of h^{\oplus} and the dissolution stops. By applying a higher anodic bias to the substrate, the energy of the h^{\oplus} increases and therefore decreases the diameter of the remaining walls producing PS with a larger bandgap. The average thickness of the silicon "wires" can be accurately controlled by the particular anodization conditions and their thickness can be further decreased by slow chemical etching in HF [1] or electrochemical oxidation [22], [23].

The model cannot, however, explain the observations of the existence of interpore dimensions as high as several micrometers in p^+ -Si or in n-Si. A modification of this model is a combination of quantum and diffusion-limited model [24]. The latter describes the mobility of carriers for the crystallites larger than 60 Å, whilst the former mobilities in smaller crystallites.

1.3 Structure of porous silicon

There is a saying in the silicon community that the bulk of the crystal was created by God, while the surface was made by the devil. Since the internal surface area of microporous silicon is of the order of $600\text{m}^2/\text{cm}^3$ [34], which makes every tenth Si atom a surface atom, it is obvious with whom one is dealing in the preparation of microporous silicon(microPS.)

V. Lehmann

The microstructure of PS can be described by an interconnected network of nanometer-size crystalline Si clusters ranging from several nm to several tens of nm in size. TEM studies show that each Si cluster is surrounded by amorphous materials such as amorphous Si or amorphous SiO_2 [26]. Infrared vibrational spectroscopy indicates that freshly prepared PS samples are composed mainly of Si, H, and O components. H and O are chemisorbed at the large internal surface forming Si-H and Si-O-H bonds. During ambient exposure, this H passivated surface is gradually replaced by an oxide surface [27]. The direct consequence of this oxidation is the replacement of Si-H bonds on the Si cluster surfaces by Si-O or Si-O-H [28], which results in a reduction of the pore size on the internal surface and of the size of the microcrystals [29]. The morphology of the porous structure is determined by the exact anodization conditions, i.e., the silicon type, the doping level, the current density, the chemical composition of a solution, the anodization time, the temperature as well as the illumination during the etching process, etc.

- From TEM it is known that the microscopic structure depends strongly on the **doping level** of the substrate. Porous silicon morphologies are usually classified by four basic groups p , n , p^+ and n^+ . Fig. 1.3 shows representative samples from each group.

For p-type silicon, the pore diameters and remaining silicon regions are extremely small and highly interconnected. The structure is homogeneous and isotropic (Fig. 1.3 a). In heavily doped porous silicon, the PS network contains pores with preferential orientation along the forming current lines, with small branches emerging from the main pores (Fig. 1.3 c). The pore and silicon cluster diameters are broadly distributed from scarcely observable for p-type silicon upto larger ones [31] in heavily doped samples. For n-type silicon at low dopant concentrations, the pore diameters are considerably larger than for p-type silicon and show strong tendency to form straight channels. The pore morphology and

Figure 1.3: Cross-sectional TEM micrographs showing the basic differences in the morphology between p, n, p^+ , and n^+ . (a) p-type silicon. Pore diameters are extremely small and highly interconnected. (b) n-type silicon. Strong tendency to form straight channels. (c) p^+ -type silicon. Tendency to form small 5-10 nm channels with numerous side branches. (d) n^+ -type silicon. Virtually identical to p-type silicon. The current direction for all samples is from bottom to top and the anodization conditions are 49 % HF at 10 mA/cm^{-2} [25].

diameters of n^+ and p^+ porous silicon are comparable [25].

- The microscopic structure depends not only on the doping level of the substrates but also on the **current density**. Generally, an increase in the current density is accompanied by an increase in the pore diameter for both n-type and p-type silicon, although the effect is more pronounced for n-type silicon resulting in larger pore diameters. (Details of the influence of current density on a PS structure are described in chapter 5)
- Another important sample parameter is the layer thickness of the PS films, which depends strongly on the **etching time**. A rise of anodization time causes an increase in the layer thickness [30] as well as the additional thinning of the remaining nanocrystals [31] as a result of chemical dissolution of porous layer in HF.
- A Raman study of porous silicon [30] indicated that the size of the Si cluster (or column) can be controlled by **HF concentration**, i.e., it decreases with a decrease in chemical composition concentration. Further, an IR study showed that for a lower concentration the optical thickness of PS is smaller. This means that the porosity of PS sample increases with a decrease of HF concentration. Similar results were obtained by electron microscopy [18] (for details see chapter 5).

Although the resulting pore structure can be quite complicated, with the porous silicon crystal lattice being highly strained in an asymmetric fashion [32], it is interesting to note that the silicon remaining retains its original crystallinity [33], indicating that pore formation occurs by a direct dissolution (see chapter 2.1) of the bulk material, and is connected with some redeposition or restructuring process.

1.4 Luminescence

Bright visible luminescence at room temperature from porous silicon after photo- or electroexcitation is an exciting phenomenon, not only from a fundamental standpoint, but also due to its promise of technological application.

1.4.1 Photoluminescence

The room temperature photoluminescence of porous Si in the visible region was first reported by Canham [1]. The typical photoluminescence peaks between 1.6-1.9 eV and have a half width of 0.3-0.4 eV. The exact position of the peak depends on fabrication conditions and subsequent treatments. The absorption is also found to depend on the structure of the porous sample. The luminescence excitation, which generally coincides with absorption in a semiconductor, begins at 2.4 eV and its threshold stays relatively constant [35]. Kanemitsu et al. [36] observed a large Stokes shift of ~ 1 eV between the photoluminescence peak and the edge of the excitation spectrum of PS, the latter was found to be about 3.2 eV. The photoluminescence excitation spectroscopic measurements by Wang et al. [35] showed similar results. For example, peak positions of the photoluminescence and the photoexcitation are at 1.8 eV and 3.1 eV, respectively. This apparent contradiction between excitation and absorption is probably due to the non-homogenous nature of porous Si material.

Recent studies [37], [38], [39], [40], [41] and [42] have provided evidence that porous silicon can luminesce in three distinct bands: the originally discovered "red" band [1] (1.5-1.9 eV), the high energy "blue" band (2.6-2.9 eV) and the infrared band at ~ 1.18 eV [43]. Red and blue luminescence are affected by oxidation of PS in different ways: the blue band appears after oxidation [40], [41], [42], whilst the red band, which is already present in as prepared material becomes stronger upon oxidation of the PS. After heavy oxidation, however,

the red band tends to vanish [42], [44]. Several authors have reported that post-anodic treatments of porous Si, like thermal oxidation could shift the PL spectra to a shorter wavelength [45], [21], [46]. It has also been reported that the peak wavelength shifts to shorter wavelengths with extending exposure time [47], [27]. As mentioned above, the emitted energy depends on the fabrication conditions, i.e., an increase of the anodization current density [48] or extending electrochemical etching time [49] could shift the PL spectra to higher energies. Using a post-treatment of light-emitting porous Si in boiling water a blue-green light emission at a wavelength of 500 nm was reported by [50]. Recently, a very intense violet emission has been observed at a wavelength of 415 nm from an anodized thin μ -Si film [51].

The decay characteristics of PL also indicate the non-uniform nature of luminescence and could be distinguished by slow and fast luminescence decay for red and high energy "blue", respectively. The fast decay is reported to range from subnanoseconds to several nanoseconds, depending on the temperature [48], [52]. Luminescence is dominated, however, by the "slow" decay. There is some controversy in the literature as to how long this takes, [28] reports decay in the range 1-50 μ s, whereas Bsiesy et al. [23] found a range 5-100 μ s at room temperature. The maximum of the red PL band observed within 1-10 μ s from the moment of excitation shows a linear blue shift with decreasing temperature from 300 K to 30K. Conversely, the luminescence observed after 30-100 μ s has complex temperature dependence above 150 K. Studying the PL decay behaviour, different groups have found very different time constants (varying from 100 ps to 1 ms) and also different decay (exponential, double- exponential, and mainly stretched-exponential, and other nonexponential) functions [52], [53], [54]. The stretched-exponential decay function [55] is given by:

$$I(t) = \alpha e^{-(\frac{t}{\tau})^\beta}$$

where α is an amplitude at $t=0$, τ a mean lifetime, and β describes the dis-

tribution of lifetimes and ranges from 0 to 1. The nonexponential decay is characterized by several time constants attributed to either an energy distribution of localized states or a distribution of escaping tunneling times out of quantum dots or hopping among sites distributed on a disordered lattice. The nonexponentiality increases with the increasing PL photon energy [53] and the decay times become shorter with decreasing emission wavelength (or increasing energy) [38], [40], [41].

The infrared (IR) band has been found at low temperatures (about 4.2 K). Its quantum efficiency increases with decreasing temperature [56], [57], and the decay time of IR lies in the μs range.

Degradation

The problem of using porous silicon in optoelectronic device structures is

Figure 1.4: Influence of UV light on the photoluminescence of as-prepared sample (our own measurements).

its degradation behaviour. Some groups [58], [59],[53] have observed the decrease of PL intensity parallel to the decrease of $Si - H_2$ content in their thermal treatment experiment. In the photo-oxidation study, Tischler et al. [60] have found a decrease in both PL intensity and lifetime which may be due to dangling bond formation. The degradation of the photoluminescence has also been reported under photoillumination [61] and mechanical stress [62]. In Fig. 1.4, the degradation behaviour of the photoluminescence of as-prepared sample under UV radiation (366 nm) is shown. As can be seen the peak intensity decreases with extending time of UV illumination, but the spectral shape and peak wavelength do not change. This change in photoluminescence intensity with illumination time is inferred to be associated with the additional oxidation of PS sample [60].

1.4.2 Electroluminescence

From the both a fundamental and technological standpoint, it is very important to determine whether or not visible electroluminescence (EL) can be achieved from PS-based devices.

Solid-state electroluminescent devices have already been fabricated from PS [63], [64]. For example, there have been some reports of visible electroluminescence from solid-state light-emitting diodes (LEDs) such as semitransparent Au/PS Schottky junctions [63], [64], indium tin oxide (ITO)/PS [65], [66], and microcrystalline silicon carbide (μc -SiC)/PS pn junctions [67]. However, the their quantum efficiencies are very low ($< 10^{-4}$). One of the difficulties with observing efficient electroluminescence from PS is related to electrical contacts. Producing appropriate contacts for PS is complicated by the porosity and inherent inhomogeneity of the material. To date, the most efficient EL (about 0.1 %) phenomena have been obtained in liquid phase structures (aqueous electrolytes) [22], [68]. This is so-called wet elec-

troluminescence, as opposed to the solid electroluminescence [64] obtained by solid contact at the external surface of the porous layer. In liquids, the carrier injections takes place through the developed surface of the porous silicon. However, it is almost impossible to use this technique to fabricate Si integrated circuits. Quite recently, electroluminescence in a scanning tunneling microscope (STM) has been observed, stimulated by the high current densities that can be provided by the probing tip when operating in the point-contact regime [69].

The color of emitted light is seen to change from dark red to bright green as the voltage is increased [148]. It is notable that this visible light emission after electro- and photoexcitation is comparable with each other. This indicates that the same basic mechanisms can be at the origin of the two signals [70].

1.4.3 Cathodoluminescence

Cathodoluminescence (CL) is a widely used technique to study semiconductors and other solids [71]. This technique is similar to the electroluminescence process in because it involves the generation of luminescence by the injected electron. The great advantages of CL are its high spatial resolution features and absence of electrical contacts. For semiconductors, the CL spectrum is very often similar to the PL spectrum. However, in the case of porous silicon, the CL spectra were different from the PL spectra measured on the same samples. The CL spectra of PS were usually composed of several well defined peaks of varying width and intensities, ranging from deep blue to the near infrared. It has been found, that the CL of porous silicon consists mainly of three bands: at ~ 750 nm (1.65 eV) [42], ~ 650 - 670 nm (1.9 eV) [42], [72] and deep blue luminescence at ~ 460 nm (2.7 eV).

The peak around 750 nm is attributed to a recombination of a quantum-confined carriers in crystalline Si nanostructures. The two other bands ob-

served at 1.9 eV ("red band") and 2.7 eV ("blue band") are well known in amorphous SiO_x [73],[74], [75]. The 1.9 eV band is assigned to NBOHC (non-bridging oxygen hole center) and trivalent silicon [76], and the peak position of this band shifts with the OH content [77]. Electron bombardment induced defects such as NBOHC [1]. It is, therefore thought that the intensity of the 1.9 eV band should increase by inducing NBOHC formation using irradiation. This effect has been observed [72] for CL bands at 1.9 eV in porous samples. Conversely, Mitsui et al. [78] have reported decreasing intensity of peak wavelength of about 660 nm with electron beam irradiation. They have also found, that the decay of the 660 nm band peak intensity quickens with increasing accelerating voltage and decreasing temperature. The peak at 420 nm ("deep blue") occurred after using higher accelerating voltages. This band showed little change under variation of the electron bombardment time. These facts indicate that the origins of the two bands of luminescence 1.9 eV and 2.7 eV are different. It was suggested that the blue luminescence band originates defects in amorphous SiO_x . The 2.7 eV band has been attributed in SiO_x to the triplet luminescence of twofold coordinate silicon [75] or self-trapped excitons in an oxygen vacancy [80]. Both the above models rely on the fact that the impinging electrons have far more energy than the exciting photons and are thus capable of exciting large-gap SiO_x (PLE peak energy ~ 5 eV) [75]. In contrast it is the low energy photons that dominantly in the excitation of silicon nanocrystallites. This shows that CL can arise from both phases: defective SiO_x [81], [79] and from the porous Si across the entire visible range [82].

1.5 Luminescence mechanism models

An understanding of the physics underlying the origins of PL activity is still subject to controversy for the development of porous silicon (PS) for device

fabrication. Several physical models have been proposed, including quantum confinement effects in narrow undulating wires and/or crystallites, the luminescence from SiH_x [60], [83], siloxene and its derivatives [84] or polysilanes [85] or finally hydrogenated amorphous Si [86]. These models are successful in describing certain specific cases, but fail to give a general explanation of all PS luminescence phenomena.

1.5.1 Quantum Confinement

It is well known that in a small-scale semiconductors electron confinement results in an effective increase of the band gap [88], [89]. This occurs because the electron and hole acquire in small crystallites (quantum crystallites) a significant quantum energy of localization which increases the recombination energy. The increase of the band gap in the "quantum dots" has been reported for physical phenomena such as optical absorption [90], photoemission [91] and others. Isolated Si nanoparticles in a SiO_2 matrix also display a similar blue shift with decreasing size [92]. Also, the studies of the structure by small-angle X-ray scattering (SAXS) from light-emitting porous silicon [93], by TEM and Raman studies [29] show correlation of the size of Si crystallites with PL and FTIR measurements. Furthermore, extensive etching studies revealed a strong dependence of the peak position of the luminescence on porosity which could be controlled by treatments subsequent to the initial etching. Finally, the quantum-size effects have also been invoked to explain the observation of visible luminescence in various systems containing silicon nanocrystals, which have been produced by techniques other than etching [94]. Thus it seems reasonable to suggest that these Si nanostructures might be responsible for the luminescence [1].

A large amount of experimental results, however, cannot be explained by

the use of this model alone. The large PL FWHM as well as a large distribution of luminescent decay time is typically attributed to distribution of different cluster sizes [28]. Since the probability of the transition of larger clusters (radiative decay rate is inversely proportional to fifth power of cluster size) to the Gaussian shape PL is extremely small, hence a very strange size profile distribution is implied. Furthermore, the existence of the fast decay (subnanoseconds order) [36] requires the presence of extremely small clusters which do not match the observed emission wavelength. Also, the temperature dependence of PL intensity is not understood by considering the quantum size effect as the origin of PL. According to the quantum confinement model (QCM), the PL peak positions should redshift with increasing temperature because the indirect band-gap of Si decreases with increasing temperature. Zheng et al.[95] and Xu et al.[59] reported independently both blue and red shifts with increasing temperature. Under hydrostatic pressure, the PL peak showed a blueshift at the beginning but appeared to be constant or even exhibited a small redshift above 20 kbar [96]. This is contrary to the fact that the indirect gap of Si decreases with increase of pressure [97].

The complex mechanism of PL is represented by a lower energy absorption threshold than the PL peak energy. PL excitation energy is, however, always higher than PL energy. Hence, the presence of the quantum size effect is probable in porous Si absorption but luminescence should not be directly connected with this effect (see chapter 5).

A promising approach is the proposed extended model, in which the quantum confinement effect is applied in conjunction with a chemical passivation of residual Si-defect states localized at the surface [98], [99].

1.5.2 Specific compounds at inner surfaces

Alternative theories proposed that photoluminescence arises, not in crystalline Si, but in different chemical species. These make use of the experimental observations [59], [28], that hydrogen, fluorine, oxygen, carbon, etc, exist in several forms in the voids of porous silicon chemisorbed to the inner surface .

Siloxene

One of these alternative theories suggests that the luminescence is due to the presence of siloxene or its derivatives [84], [100]. Annealed siloxene $Si_6O_3H_6$ is a particular substoichiometric silicon oxide, whose idealized structure is shown in Fig. 1.5. It consists of sixfold Si-rings linked by oxygen bridges to

Figure 1.5: The idealized structure of annealed siloxene $Si_6O_3H_6$

form a two-dimensional layer. In addition, each Si atom is bonded to one H atom in order to satisfy the fourfold coordination of Si. It is quite interesting to note that there are Si magic numbers (2, 6, 10, ...) [15], at which

Si microclusters are stabilized. Siloxene obeys this criterion, so it can be postulated that 6 membered Si rings may be preferentially produced during anodic dissolution of c-Si [101]. The Si_6 acts as the colour center, giving rise to strong luminescence of siloxene at room temperature. The fluorescence bands emitted by siloxene can be tuned (Fig. 1.6) in a well controlled way over a large spectral range via chemical substitution of hydrogen by other monovalent ligands such as halogens, OH or alcohol groups [102]. The oxygen lone pair moreover, plays an important role in determining the character of the valence band [103]. Alternatively, tuning can also be achieved by annealing of siloxene in air. This leads to interlayer cross-linking in the siloxene complex via the formation of Si-O-Si bonds and the evolution of H_2O [104].

Polysilane

Polysilane has been proposed as the luminescent substance because the infrared absorption spectroscopy studies show that the inner surface of porous Si is passivated by hydrogen [107]. The fact that with increasing temperature, hydrogen desorption is observed together with decreased PL intensity also supports the model. Polysilane is a Si-skeleton material and its one-dimensional and two-dimensional versions were identified as specific compounds at the porous Si surface [108]. Chemically synthesized polysilanes also show the visible luminescence [86].

1.5.3 Amorphous structure: $a-Si:H$, $a-SiO_x:H$

It is known, that $a-Si$ and $a-SiO_x$ produce various luminescence in the range from infrared to visible [109]. Since amorphous structure is observed in porous Si, it is natural to consider the amorphous layer to be a luminescent substance. The luminescence characteristics are quite similar to those of PS,

Figure 1.6: Tuning of colour of luminescence via chemical substitution of halogen and OH groups [106]

in the sense that they have a broad range of decay times as well as a large half width. This is due to the fact that in amorphous Si, the luminescence originates from spatially separated electron-hole recombination on the band tail states [110]. Also, the quantitative similarities in the dynamic room temperature behaviour of porous silicon layers obtained from either $a-Si:H$ or Si wafers suggest that the nonradiative PL quenching has the same origin in both materials [111]. The typical luminescence of $a-Si:H$ peak is at ~ 1.4 eV, but it can shift into the visible light range if the concentration of H

is increased. From Raman and ellipsometry measurements it has been found that at temperatures around 400°C an amorphization of the porous layer takes place [77].

1.5.4 Surface states

Since a surface can also have a strong effect on semiconductor behaviour, and as porous silicon has an enormous surface area between 200 and 1000 m^2 for each cubic centimeter of the material, many researches [112] believe that the surface is responsible for the efficient luminescence. They suggest

Figure 1.7: Configurational coordinate diagram and possible photoluminescence process in porous Si. Bands for an electron-hole pair in a Si nanostructure and bulk Si, an excited state of a luminescence center and a ground state are shown as a function of the configurational coordinate, q , related to the local lattice distortion around the luminescence center [113].

that the enlarged bandgap of porous silicon is a quantum size effect, but its crystalline skeleton has an imperfectly passivated surface as a result of its

irregular shape and the strained bonds between silicon atoms at the surface. This might lead to that, that surface states produce luminescence. This process is illustrated by a configurational coordinate diagram [114], as shown in Fig. 1.7, where excited luminescence centers and the ground state are shown as a function of a configurational coordinate q related to the local lattice distortion around the luminescence center. The electron-hole pair trapped and localized at the excited luminescence center through the local lattice distortion, recombines radiatively through the transition from the relaxed, excited luminescence center to the ground state without any change in q according to the Franck-Condon principle. Therefore, the luminescence band is described by Gaussian-like shape with a large full width at half-maximum for the vibration of atoms around the luminescence center.

The surface trap states and extended states in the PS clusters are involved in the visible light emission of PS in the red/orange region. The blue-green luminescence is likely to be related to emission from the defect centers in oxygen-deficient silicon oxide SiO_x (2.7 eV) and to adsorption/desorption of OH on the Si nanostructures (2.25 eV) [40], [115].

Chapter 2

Experimental data

2.1 Preparation of porous silicon layers

All results presented in this thesis were obtained on porous silicon films prepared by the electrochemical anodization process. Fig. 2.1 presents schematically the anodization Teflon cell used for PS formation. The Si wafers served as the anode and are mounted on the Cu-plate. We have mainly used for PS formation the p-type (100) silicon substrates (boron-doped) with resistivity of $10 \Omega \cdot \text{cm}$. Before anodization process, the Si samples were cleaned in an ultrasonic bath for 2 minutes. To ensure a good electrical contact, a Pt coating was evaporated on the backside of the wafer before etching. The cathode was a plane spiral platinum wire, parallel arranged with respect to the Si-wafer. The electrolyte for the PS formation was mainly a mixture of 40% HF, water and ethanol. A constant current source was used as a power supply for the electrochemical process. Silicon is inert in the HF solution, but when a positive (anodic) voltage is applied to silicon wafer being in contact with HF solution, its surface is either electropolished or turned into a porous film. The etching process was carried out under constant current conditions at room temperature and in the dark. This type of cell is commonly used

Figure 2.1: Schematic presentation of the anodization cell for the PS formation.

due to good uniformity of formatted PS layers and control of current-voltage characteristics.

2.2 Measurements of optical properties

2.2.1 Photoluminescence and Excitation

The PL (photoluminescence) and PLE (excitation) measurements were taken with a Shimadzu RF-5001 PC spectrofluorophotometer at room temperature. The spectra were corrected for the apparatus response. In a PLE experiment, one varies the wavelength of the excitation light and monitors the change in PL intensity at a fixed wavelength. Conversely, in PL measurements, the excitation wavelength is fixed and one monitors change in the PL intensity

with variation of wavelength.

2.2.2 Time-Resolved Spectroscopy

The setup (Fig. 2.2) for measurements of time-resolved spectroscopy consists of an Argon Ion Laser (Ar, cw 8W) which pumps the Titan Sapphire (Ti:Sa) laser. The Ti:Sa laser creates light of a wavelength of about 800 nm with a bandwidth of about 15 nm. The Ti:Sa light is pulsed with a frequency

Figure 2.2: Experimental set-up for measurements of time-resolved spectroscopy.

of 76 MHz and a pulse length of 100 fs. To get a longer pulse-to-pulse time, the repetition rate is divided by a pulse-picker (PP) by a factor of five. This laser light is then frequency doubled by a BBO crystal to reach the desired excitation wavelength of 400 nm. Then the laser beam reaches the sample (S) via a mirror. The fluorescence light of the sample is collected perpendicular to the laser beam by a lens system (L1, L2) and directed to a monochromator (M) and a streak-scope (SSC). With the Streak-Scope we get a time resolution of about 50 ps.

2.3 Structural measurements

2.3.1 Scanning Electron Microscopy

The idea of a scanning electron microscope was proposed in 1927 by H. Stintzing [117] and the first experiments were performed by M. Knoll in 1935 [118]. However, the first commercial SEM from the Cambridge Instruments Co., Ltd., came onto the market thirty years later.

Fig. 2.3 shows the schematic view of the SEM. An electron probe is finely focused by electromagnetic lens system consisting of one or two condenser lenses and, below them, an objective lens, is scanned across the sample by means of deflection coils. The signal arising from the electron-specimen interaction is detected, amplified, and used to modulate the intensity of a TV monitor screen, which is scanned at the same rate as the electron probe. By the electron-specimen interaction, different radiation signals (secondary and backscattered electrons, Auger electrons, cathodoluminescence (for details see section 3.3.2) and X-ray radiation) are emitted from each scanned point of the sample surface. The most important for SEM imaging are slow secondary electrons (SE, ≤ 50 eV) and faster backscattered electrons (BSE, 50 eV- probe energy) [119]. The signal then controls the brightness of indivi-

Figure 2.3: The schematic view of the SEM system

dual pixels on the TV monitor screen, related to the location of the original points on the sample surface. The resolution of SEM is determined by the probe-forming lens in the SEM (e.g., 3 nm at 15 keV [120]).

In the thesis, the samples were investigated using a SEM Philips 515 operated mainly at 30 keV in energy and with a current density of $3A \cdot cm^{-2}$ at room temperature. Before SEM measurements, the PS sample surface was coated by a DC-diode sputtering system according to [121] with Pt in order to avoid electrical charging of low conducting samples, which can be induced by the incident electron beam.

2.3.2 Cathodoluminescence Mapping

Analogous to optical excitation, the electron beam bombardment enables the investigations of semiconductors. The energy of excited electrons is much larger than that of the emitted photons what enables the excitation of large-gap semiconductors. This CL technique combined with SEM is a promising method for investigations of a localized luminescence distribution because of its high spatial resolution. This technique also gives information on distri-

Figure 2.4: The schematic diagram of the CL experimental system

bution of luminescence centers along the depth of incident electrons, since it depends on accelerating voltage. However, the problem is that electron beam irradiation causes a decrease of luminescence intensity more significant than

the irradiation of light, which is due to creation of nonradiative centers such as point defects, or to destruction of luminescence centers.

Our cathodoluminescence (CL) system is based on a modified commercial scanning electron microscope (SEM) Philips SEM 515. Fig. 2.4 shows a schematic diagram of the system for CL measurements. This incorporates a collecting mirror inside the SEM chamber, which directs collected light to a photomultiplier. The photomultiplier output is fed to the data acquisition and display software in a dedicated PC type computer via A-D converter. The acceleration voltage V_a can be varied from 30 kV down to 1 kV, enabling the adjustment of the depth of the information as well as lateral resolution of CL imaging. The whole system is operated under a computer control giving the possibility to perform imaging in both secondary electron detection usual for SEM and the cathodoluminescence mode. The measurements of the CL do not require any specimen preparation with except of coating mentioned above in section 3.3.1, and they provide a fast two-dimensional (in plane) view of luminescent properties of the structure with lateral resolution about $1\text{ }\mu\text{m}$. Our system for CL mapping is able to detect the radiation from 350 nm to about 700 nm.

2.3.3 Transmission Electron Microscopy

Transmission electron microscope (TEM) [122] is very similar to the conventional light optical microscope in terms of optical principles. Fig. 2.5 shows a schematic view of the TEM. Primary electrons are emitted from an electron beam source and followed by double condenser lens system to provide uniform illumination of the specimen. The sample is mounted on a stage to provide suitable movement. The primary image is formed by the magnetic objective lens. The quality of objective lens determines the resolution of TEM (typical $\approx 0.3\text{ nm}$ at 100 keV [120]). The objective aperture, placed at

Figure 2.5: The schematic view of the TEM system

the back focal plane, controls the image contrast. To obtain bright and dark field images, the objective lens aperture has to be placed in this way, that only the undiffracted primary electrons or those diffracted in a Bragg beam are used to form the image (Fig. 2.5 (left side)). In case of the high resolution image it is necessary to use as much Bragg-beam as possible to form the image, which is achieved by removing the objective lens aperture or by applying the wide objective lens aperture. If all electrons are passed through the objective aperture (Fig. 2.5 (right side)), then the electron diffraction pattern can be observed by imaging the back focal plane of the objective lens. Electron diffraction pattern provides information about the degree of crystallinity, the orientation and crystal structure of the sample. The final image is projected onto a viewing screen through two or more projection lenses, which magnify the image onto the screen.

The TEM is usually used to study the internal microstructure and crystal structure of samples which are thin enough to transmit electrons with a relative low probability of energy loss. This requires, in contrast to SEM investigations, the corresponding sample preparation, e.g. thickness of samples in the range 20-200 nm (the 100 keV TEM), depending on the average atomic number of the material [120].

For our TEM investigations, cross sectional as well as lateral thinned samples have been prepared by mechanical grinding and polishing and subsequent ion beam milling with 3 keV Ar^+ . The TEM images were taken with a Philips CM 20 FEG using an electron energy of 200 keV.

2.3.4 Scanning Tunneling Microscopy

In contrast to conventional electron microscopy, scanning tunneling microscopy (STM) can be performed in air, liquids and in vacuum [123]. Fig. 2.6 shows the schematic diagram of the scanning tunneling microscope. A probe

tip is usually attached to a piezodrive, that consists of three piezoelectric transducer X, Y, and Z piezos. Using the stepper motor (coarse position-

Figure 2.6: The schematic diagram of the STM.

ing) and the z piezo, the tip and sample are brought to within a few Å of each other, resulting in a significant overlap of their electronic wavefunctions. Upon applying a bias voltage, the electrons from the occupied electronic states near the Fermi level of one electrode can "tunnel" across the narrow gap (0.5- 1.5 nm) [120] into the unoccupied states of other electrode. The flowing tunneling current can be described for one-dimensional case following [124] :

$$J_T = U_T \exp\left(-\sqrt{\frac{2m_e\Phi}{\hbar^2}}d\right) \quad (2.1)$$

where d represents the tunnel distance, U_T - bias potential between tip and sample, and Φ is the effective barrier height between the two electrodes.

By using piezo drive system for the tip and a feedback loop which controls the tunnel current at a constant (mean) value, one can obtain a map of surface topography or an atomic resolution image. In the former, the tip is scanned

Figure 2.7: Scanning tunneling microscopes can be operated in either the constant current mode (left side) or the constant height mode (right side) [129].

over a surface while the current I_T , between it and the surface, is kept at a fixed value. A feedback network changes the height of the tip z to keep I_T constant. An image consists of a map $z(x, y)$ of tip height z versus lateral position x, y . This is the constant current mode of operation [125], [126], [127]. In the latter case (Fig. 2.7, right side) the constant height mode [128], a tip is scanned across a surface at nearly constant height and constant voltage while the current is monitored. In this case the feedback network responds slower but rapidly enough to keep the average current constant.

2.3.5 Scanning Electrochemical Tunneling Microscopy

As mentioned in section 3.3.4, the STM can also be performed in liquids. In 1986, Sonnenfeld and Hansma showed for the first time that high resolution images can also be obtained in electrolyte solution [132]. The next important step was the introduction of the potentiostatic STM concept reported

by several groups [133], [134], [135]. This allows the diminution of unwanted electrochemical processes at the electrode during and between STM imaging. The schematic view of a potentiostatic STM concept is illustrated in Fig. 2.8.

Figure 2.8: Schematic presentation of SECM. The tunneling voltage U_T is defined by the difference of E_T and E_S . I/V=current/voltage converter for measuring I_T . Potentiostat P controls indenpendently E_T and E_S [131]

The potentiostat consists of a floating operational amplifier P, connected to sample S and tip T via two floating low-impedance voltage supplies V_S and V_T . The potential E_S of the sample vs. the reference electrode is adjusted at V_S . V_T can be defined either as the potential E_T vs. the reference electrode or the tunneling voltage $U_T = E_T - E_S$ between tip and sample. The electrochemical current I_S at sample is measured as the total current $I_T + I_S$. This means, that under idealized condition, the electrochemical processes at both electrodes (sample, tip) can be controlled separately by a potentiostatic concept [133], [134]. However, we cannot diminish the electrochemical charge transfer reactions which can cause arbitrary changes in surface morphology and the chemical composition of both tip and substrate by adsorption and

phase formation/dissolution processes. To achieve optimum reduction of the electrochemical tip current, the proper tip materials should be chosen, that is chemically inert in the given solution. Owing to development of appropriate tips coverage, except for the very end of the tip, by thin insulating layers, thereby minimizing faradaic currents and chemical processes on the tip [136]. This is usually done by applying insulating coatings to tips with a tapered end shaped mechanically or by electrochemical etching (for details see [136]).

Chapter 3

Evidence of Anisotropic Structures of Free Standing Porous Silicon layers.

The first idealized model of light-emitting porous silicon (PS) was a system of nanowires, oriented in the $\langle 100 \rangle$ direction [25]. Numerous subsequent microstructure investigations failed, however, to replicate this early model. SEM, TEM and other methods did not find any preferential direction in the Si cluster distribution and describe the PS structure as sponge or coral-like, that is more or less isotropic. To our knowledge there is no evidence for the anisotropy of the physical properties of the PS structure existing in the literature, save for a small 4% anisotropy in the refractive index [192]. In spite of the fact, that the PS has been extensively studied, there is no consensus as to its degree of ordering on an atomic scale: some authors consider it to be mainly amorphous [193], [194], whereas others prove Si crystalline structure being preserved [195], [94], [158].

Considering now the macrostructure, one can see great progress has been made in the understanding of the macropore formation mechanism, based

on the use of the self-adjusting model proposed by Lehman [196], [197]. Free-standing PS films are of great interest, because they offer the possibility to study PS properties with techniques, which cannot be applied to the PS films on Si substrate (optical absorption in visible range, conductivity, etc.). However, the fabrication of free-standing films of sufficient size is a delicate procedure, due to their poor mechanical strength. High porosity light-emitting material makes the task even more complicated [197]. As a result, the number of publications, devoted to PS separated from substrate is much less than that for PS layers on Si [198], [199], [200], [201], [203]. Optical and secondary electron beam images of free standing porous silicon films reveal a pronounced layered structure [202]. Films tend to split into sheets parallel to the (111) plane of the initial substrate and form steps and terraces at the broken edge of the film. We have investigated these layers by scanning and transmission electron as well as optical microscopy. We have not observed any significant differences in the porous structure of each layer. Film layering in the cross section view, caused by these terraces, has a periodicity of about $1\text{ }\mu\text{m}$. The origin of this effect is discussed and could arise from the electrochemical etching regime used vertical inhomogeneities in the starting material or mechanical stress related effects arising from electrolyte evaporation.

3.1 Description of samples

The porous layer can be removed from the substrate by applying a high current pulse at the end of the electrochemical treatment [204]. However, the preparation of large, high quality films in this way is difficult. The free-standing porous silicon films described in this chapter were produced by electrochemical etching of an epitaxial $p - p^+$ (111) Si substrate. The top epitaxial layer had a resistivity of $\rho = 2.5\text{ }\Omega\cdot\text{cm}$ and was about $10\text{ }\mu\text{m}$ thick.

The monocrystalline Si substrate, doped with boron to $\rho=0.03 \text{ } \Omega\cdot\text{cm}$, was cut from a 76 mm diameter Czochralski grown crystal. Anodic etching was carried out in $HF + H_2O$ mixture (1:1) under a constant current density of $150 \text{ mA}\cdot\text{cm}^{-2}$ for 25 min. During the final stage of the etching process, a current density of $300 \text{ mA}\cdot\text{cm}^{-2}$ was applied for 30 s, to separate the PS film from the substrate. Subsequential rinsing with de-ionized water was carried out and drying took place in ambient air. The films were predominately a transparent yellow colour and approximately $80 \text{ } \mu\text{m}$ thick. The face surface was concave due to mechanical tensions, which are higher in the upper part of the film. Free-standing films demonstrate high chemical reactivity, even reacting with deionized water and dissolving therein within two days. Sometimes the drying process of the films was accompanied by breaking, crashing and even sparks. Light-emitting films show more intensive red luminescence from the front side than from the back, when excited with the UV radiation of Hg lamp. Images were obtained with a video camera attached to a light microscope and a (SEM) Philips 515 (see chapter 3.3.1) operated at 30 keV in energy and with a current density of $3 \text{ A}\cdot\text{cm}^{-2}$ at room temperature. For the TEM investigations (see chapter 3.3.3), cross sectional as well as lateral thinned samples have been prepared by mechanical grinding and polishing and subsequent ion beam milling with 3 keV Ar^+ . The TEM images were taken with a Philips CM 20 FEG using an electron energy of 200 keV.

3.2 Results and Discussion

Both light-emitting (high porosity) and nonemitting free-standing films have a layered structure. The scanning electron microscopy and light microscopy images of the macrostructure of the PS sample in Fig. 3.1 show a staircase-like structure. When broken into pieces, the films had a tendency to split into planes, forming steps and terraces at the edges, reminiscent of

Figure 3.1: Light microscopic (a) and SEM (b) image of free-standing PS sample.

the behaviour of mica. On the top of the film there is a thin separated sheet, divided into small parts, which are rolled like papyrus. This layer shows the brightest light emission. It is interesting to note that there are no significant differences in the thickness (about $1\ \mu\text{m}$) and the microstructure of each layer in the cross section SEM images Fig. 3.2. Each layer has a porous structure quite similar to that which was reported earlier for PS layers on the Si substrate [156]. The diameter of the pores is about 20-30 nm, as shown in Fig. 3.3 a, b and Fig. 3.5 a, respectively. We have not observed any significant changes in the nanostructure of each layer. The threadlike structure had the same density in every layer and displayed little structural changes. Furthermore, high resolution TEM studies (Fig. 3.4 a) show that the remaining crystalline Si is surrounded by amorphous material, possibly amorphous SiO_x .

Although the resulting macrostructure is quite complicated and highly strained in an asymmetric fashion, we have found that the remaining silicon retains its original orientation. This can be seen from the diffraction pattern

Figure 3.2: Cross section SEM images of the angle at the edge of the film (a, b, c) and of a side of the edge (d) pictures correspond to different magnifications, as indicated in the figures

in the Fig. 3.4 b and Fig. 3.5 b, respectively. A weak distortion of the orientation is indicated by a tangential broadening of the diffraction spots. The broadening corresponds to a misorientation of $\pm 3^\circ$ in plan view and $\pm 1^\circ$ in cross section, i.e., around $\langle 111 \rangle$ and $\langle 110 \rangle$, respectively. This is suggestive of the presence of the internal stress.

Furthermore, the free-standing PS sample prepared at different current density also shows the layered structure, but the thickness of the layer is about $20 \mu\text{m}$. Fig 3.6 shows the free standing PS sample prepared at a current density of $60 \text{ mA}\cdot\text{cm}^{-2}$ for 35 min and finally etched at a current density

Figure 3.3: Transmission electron bright (a) and dark field (b) images

Figure 3.4: High resolution transmission electron micrograph (a) and a related diffraction pattern (b) of a free-standing PS film in plan view, lattice fringes correspond to Si [220] planes with a spacing of 1.92 \AA . The diffraction pattern is related to the $\langle 111 \rangle$ direction oriented parallel to the electron beam.

Figure 3.5: Transmission electron bright field (a) image and a related diffraction pattern (b) of free-standing PS film in cross sectional view. The diffraction pattern is related to the $\langle 110 \rangle$ direction oriented parallel to the electron beam.

Figure 3.6: The cross-sectional SEM image of free standing PS films prepared at a current density of $60 \text{ mA}\cdot\text{cm}^{-2}$ for 35 min and finally etched at a current density of $120 \text{ mA}\cdot\text{cm}^{-2}$. Each layer is $\sim 20 \text{ }\mu\text{m}$ thick

of $120 \text{ mA}\cdot\text{cm}^{-2}$ for 30 s (p^+ , $\langle 100 \rangle$ Si substrate, resistivity of $\rho = 1 \text{ }\Omega\cdot\text{cm}$, $\text{HF} + \text{H}_2\text{O} + \text{C}_2\text{H}_5\text{OH}$ mixture (2:1:1)).

It is well known that Czochralski-grown monocrystals may have stripes of resistivity and microdefects in the growth direction [207]. These are formed due to fluctuations of the crystallisation rate and may be observed in the crystal cross section after a special etching process, as stripes parallel to the $\langle 111 \rangle$ plane. Anodic etching of silicon is very sensitive, not only to the defects, but to the doping level as well. It is used to detect defects [208] or to form superlattices from the structures with various doping levels along the etching current direction [209], [210]. The p^+ layers are attacked and show high porosity, while p^- regions show low porosity. Porosity and mechanical strength are tightly interrelated and sheets of alternative strong and weak planes may be formed as a result of anodic etching. It should, however, be noted, that the distance between the stripes in our experiment is too small to correspond to possible layers with various resistivities, where they should be of the order of several mm [207]. There is no visible difference in the cross

Figure 3.7: Cross sectional SEM image of the PS sample prepared with a current density of $127.5 \text{ mA} \cdot \text{cm}^{-2}$ ((100) p-type silicon substrate (boron-doped), a resistivity of $10 \Omega \cdot \text{cm}$ and a solution of HF (40% wt)+ $\text{C}_2\text{H}_5\text{OH}$ (1:1), t_A 20 s).

section images between the top part of PS film, formed from epitaxial layer, and from the p+ substrate. Hence, the effect is more likely to be related to microscopic atomic-scale defect distribution than to resistivity stripes.

However, it is also well known, that the porous silicon layers show the tendency to have a mechanically weak structure with increasing current density. This is due to higher porosity, resulting in many cracks or peeling off from the substrate [155]. Lehmann et al. [11] have reported that the PS layers cracked while drying and the pieces shrunk considerably in size. A useful analogy is that of the formation of mud cakes in a drying lake. The effect was found to be due to existence of enormous capillary tensions formed by the liquid-vapour interfaces during drying by evaporation [212] or due to a collapse of the pores under the attractive forces between the surface hydrogen atoms [11]. For current densities below $100 \text{ mA} \cdot \text{cm}^{-2}$, PS was found to dry without cracking for a layer thickness up to $10 \mu\text{m}$, which may be

due to a more stable silicon skeleton being formed at lower current densities [11]. In the case of our PS samples with a substrate prepared with a current density of $127.5 \text{ mA} \cdot \text{cm}^{-2}$, we have observed not only the tendency of cracking, but of peeling off as well. Fig. 3.7 shows a PS sample with the substrate prepared at a high current density, where this effect can be seen. The thickness of this layer is about 500 nm. This compares to a thickness of 80 μm in the case of our free-standing PS. We believe that the mechanical stresses resultant in such a thick layer will lead to similar processes as to those in the PS sample (Fig. 3.7), resulting in splitting of the porous sample into sheets. Electrochemical studies of the anodization have shown [5], [10], that the anodic process changes gradually from pore formation towards electropolishing as the current density increases. We have fabricated our samples at the transition zone, where fluctuations of the current density exist which can lead to a pore formation as well as to the electropolishing process responsible for smooth boundaries between the layers. This could be a reason for the periodicity in this observed layered structure, in the sense of some self-organized spatial pattern. Both processes, the mechanical stress and the special etching regime, could be the origin of the formation of layered structure of PS samples.

Chapter 4

Dependence of structure and optical properties of porous silicon on preparation parameters

Observation of an efficient room-temperature PL of PS has stimulated extensive research on explaining of the physical mechanism responsible for such luminescence. Luminescence and the PS structure have been studied and several models have been proposed, as described in chapter 3. Some recent results have been explained by invoking a quantum confinement/luminescence center model (QCLC) [137], based upon electronic excitation within nanoscale silicon with subsequent tunneling of excited carriers and recombination in SiO_x surface layers [138], [137], [42], [139],[99], [140], [141], [72], [142]. An important aspect of this model is that an emission spectrum from porous silicon should be characteristic for luminescence centers in SiO_x . In this case, one should expect the emission to be composed of multiple emission bands as it is seen in crystalline and amorphous SiO_2 ($a-SiO_2$) [143], [144].

Usually one observes a single PL band in PS, but in several articles the existence of two or more bands has been reported [47], [174], [115], [166], [167], [145]. The maxima of two overlapping emission bands have been shown to exist just below 600 nm and around 660 nm [47], or 680 nm [174]. TRS measurements have shown the differences in the lifetimes for each band, the 590 nm band has been observed to decay in a few μ s and the 680 nm band within a few tens of μ s [115].

In the present chapter we report on the investigations of the luminescence and structural properties of PS samples prepared at various etching conditions (variation of the current density and the HF concentration). Structural investigations have been made by SEM and STM. They offer increasing thickness of the porous layer and density of pores with an increasing HF concentration. There is, however, no visible difference either in the cross-section SEM images in thickness or in the microstructure (SEM, STM images) of surface layers of PS samples prepared at various current densities. Further, we have observed the evolution of the photoluminescence spectrum (PL) from single peak at ≈ 1.88 eV into two peaks at ≈ 1.88 eV and ≈ 2.05 eV with increasing current density. We have found that energetical positions of particular PL bands depend very slightly on their preparation parameters. The influence of Pt-coating of PS sample on PL was also studied. The PL spectra are analyzed by deconvolution into 2, 3, 4 Gaussians. It is interesting to note that the two bands (at ≈ 1.88 eV and at ≈ 2.05 eV) exist in an each deconvolution. We have also observed the systematic dependencies not only in the ratio of intensities but in the FWHM and area of the two Gaussians as well. Thus, the two mentioned above peaks can be identified as arising from radiative recombination through excited luminescence centers. We can state that there are at least two types of luminescence centres.

4.1 Sample preparation

All results presented in this chapter were obtained on porous silicon films prepared by the electrochemical anodization process of p-type (boron doped) Si (100) wafers with $10 \, \Omega \, \text{cm}$ resistivity. We have fabricated two sets of PS samples, the first set by varying the HF concentration (group 1) and the second (group 2) by varying the current density. Group 1 samples were electrochemically etched for 30 s using a current density of $14.8 \, \text{mA} \cdot \text{cm}^{-2}$. The electrolyte for the anodization was a solution of 10%, 20%, 30%, 40% HF and $\text{C}_2\text{H}_5\text{OH}$ (1:1) for individual samples 1a, 1b, 1c and 1d, respectively. For the group 2, the porous Si samples were formed by anodization in a mixture of HF (40% wt)+ $\text{C}_2\text{H}_5\text{OH}$ (1:1) for 20 s. The current density of anodization was 25.5, 51, 76.5, 102, $127.5 \, \text{mA} \cdot \text{cm}^{-2}$ for individual samples 2a, 2b, 2c, 2d, 2e, respectively.

After PL, PLE measurements and SEM investigations of group 2 samples, we evaporated a Pt layer, about 5 nm thick, onto the surface layer of the PS samples. For this purpose we have used a DC-diode sputtering system according to [121]. The detailed description of the experimental set-up for structural and luminescence measurements is given in chapter 3.

4.2 Variation of HF concentration

4.2.1 Structure analysis

The surface morphology and cross-section of the PS films were systematically investigated by scanning electron microscopy operated at an energy of 30 keV, with a current density of $3 \, \text{A} \cdot \text{cm}^{-2}$ at room temperature. Fig. 4.1 shows the cross-sectional SEM images of the PS layer for two HF concentrations: 10% and 40%. The general effects of increasing HF concentration are increasing total surface area and increasing film thickness from 60 nm (Fig. 4.1 a) to

525 nm (Fig. 4.1 b), from sample 1a (10% HF) to 1d (40% HF), respectively. Electrochemical studies of the anodization have shown that the anodic pro-

Figure 4.1: Cross-sectional SEM images of porous silicon layers for two HF concentration (a) 10% and (b) 40%

cess changes gradually from pore formation towards electropolishing as the HF concentration in aqueous solution decreases for a constant current density [5], [147]. We have observed for our samples the increase of the roughness of the surface of PS with a decrease in HF concentration. This result is consistent with the HF concentration dependence of the column or particle sizes, where the density of steps or kinks on the surface is expected to be higher for smaller particles (or columns) with diameter of approximately 2-10 nm. As we know from the Raman studies, the size of Si particles is smaller for lower HF concentration [30]. Furthermore, the IR studies have shown that the surface of those nanostructures is covered by monohydrogen and dihydrogen. The relative amount of the dihydrogen absorbed on the surface increases with respect to the monohydrogen with decreasing HF concentration [30]. The infrared measurements also show that the optical thickness of PS decreases with a decrease in HF concentration. Smaller optical thickness means larger porosity and/or thinner porous layer.

4.2.2 Spectroscopic measurements

Photoluminescence spectra of PS layers prepared with different HF concentration are shown in Fig. 4.2. These spectra show a continuous shift (0.36 eV) of the luminescence peak to lower energies with increasing HF concentration, as it is also reported in the literature [147], [155], where this effect it is normally explained in terms of the quantum confinement model. The

Figure 4.2: The room-temperature photoluminescence spectra of porous Si observed with excitation light of 366 nm for the samples 1a, 1b, 1c, 1d prepared with 10%, 20%, 30% and 40% HF, respectively. The maxima appear to be skewed towards higher energy with decreasing HF concentrations.

position of photoluminescence peak energy ranges from 1.96 eV (sample 1a) to 1.6 eV (sample 1d). The full width at half maximum (FWHM) of the spectrum increases with decreasing HF concentration from 0.38 eV to 0.43 eV, for 40% and 10% HF, respectively. This FWHM of the luminescence

spectrum of these samples is quite large compared with c-Si.

A similar continuous shift has been found [47] in photoluminescence with variation of the exposure time. The higher energy peak becomes stronger than the of lower energy peak with increasing exposure time. The PL was inferred by [47] to be associated with the changes in the structure from H-passivated to more stable O-passivated structure. It has been reported that the oxidation rate during exposure to air is higher for PS prepared with the solution of lower HF concentration [47].

Our structural measurements presented above showed that the samples prepared for lower HF concentration display the higher porosity. In accordance with the quantum confinement model (see chapter 2.5.1), the shift of luminescence band to higher energy is expected to occur for samples with higher porosity, i.e. for samples with smaller Si nanocrystals. This suggests that the quantum size effect is a likely origin of the luminescence in PS samples. However, an increase in the density of the porosity also implies an increase in the occurrence of surface chemicals and other postulated sources of luminescence.

4.3 Variation of current density

4.3.1 Structure analysis

The samples prepared at different current densities have different PL spectra and are postulated to have different microstructures. There is, however, no visible difference in the cross section SEM images in the PS film thickness (about $0.5 \mu\text{m}$) for the different current densities. Each sample has a porous structure (Fig. 4.3), quite similar to those reported earlier [156]. We have also not observed any significant changes in the microstructure of the surface layers of these samples, as measured by SEM and STM. Fig. 4.4 shows the STM images of PS samples prepared with $25.5 \text{ mA} \cdot \text{cm}^{-2}$ (left image) and

Figure 4.3: A cross-sectional SEM image of porous silicon layer of sample 2a $102 \text{ mA} \cdot \text{cm}^{-2}$ (right image). On average the microstructures of PS sample (Fig. 4.4 b) have a larger radius than those of Fig. 4.4 a; the difference being approximately 5 nm in diameter. Takasuka et al. [158] have observed by TEM threadlike structures of Si and Si crystallites in the PS layer in all the samples prepared for different current densities. The threadlike structure had the same density in all samples and showed very few structural changes. The size of the crystallites has been observed to be broadly distributed in the range from a few nanometers to a few tens of nanometers. However, the SEM images of the macrostructure of these films (Fig. 4.5) show the tendency to have a mechanically weak structure with increasing current density. This is due to higher porosity and results in many cracks or peeling off from the substrate [155].

4.3.2 Spectroscopic measurements

Fig. 4.6 shows typical PL spectra from samples prepared at different current densities. The luminescence spectrum of each sample was measured with excitation radiation of 254 nm. The PL spectra have peaks between ≈ 2.05

Figure 4.4: STM top view of porous silicon layer of sample 2a and 2d

Figure 4.5: Cross-sectional (a, b) and top view SEM (c, d) images of porous silicon samples prepared for two different current density: at $127.5 \text{ mA} \cdot \text{cm}^{-2}$ (a, c) and $25.5 \text{ mA} \cdot \text{cm}^{-2}$ (b, d)

Figure 4.6: Luminescence spectra of porous Si observed with excitation radiation of 254 nm for PS samples prepared with different current density (a) 25.5, (b) 51, (c) 76.5, (d) 102, (e) 127.5 $mA \cdot cm^{-2}$ at room temperature.

eV (≈ 605 nm) and ≈ 1.88 eV (≈ 660 nm), depending on etching conditions and relatively wide FWHM (about 0.4 eV). Both the wavelength and the shape of emission spectrum depend on the current density during anodic etching. Generally, a higher current density results in a shorter wavelength [155]. Our spectra show similar behaviour (≈ 1.88 eV and ≈ 2.05 eV for 25.5 $mA \cdot cm^{-2}$ and 127.5 $mA \cdot cm^{-2}$, respectively). Furthermore, we observe the evolution of the luminescence spectrum from single-peak at 1.88 eV into two peaks at ≈ 1.88 eV and ≈ 2.05 eV with an increasing current density. Curve (a) in Fig. 4.6 shows the single-peak PL spectrum at ≈ 1.88 eV for

Figure 4.7: Luminescence spectra of porous Si observed at two different excitation radiation of 254 nm and 436 nm for PS sample 2c prepared with a current density of $76.5 \text{ mA} \cdot \text{cm}^{-2}$

$22.5 \text{ mA} \cdot \text{cm}^{-2}$. The emission band of the sample prepared at the current density of $51 \text{ mA} \cdot \text{cm}^{-2}$ already consists of two peaks at $\approx 1.88 \text{ eV}$ and at $\approx 2 \text{ eV}$. The short-wavelength band shifts from 2 eV to 2.05 eV , for 51 and $127.5 \text{ mA} \cdot \text{cm}^{-2}$, respectively. As the current density increases, the peak at $\approx 1.88 \text{ eV}$ continuously decreases in ratio to the peak at $\approx 2.05 \text{ eV}$. If we assume that the position of the luminescence peak is not changed by current density, the two-peak luminescence spectrum should also be expected to be observed for the sample 2a. In order to explain the mentioned above luminescence spectra, we have measured photoluminescence spectra of the same samples at an excitation radiation of 436 nm . The spectra shift slightly to lower energies with longer excitation wavelength (about 5 nm), but show the same evolution of peak structure. However, we observed a small change in the ratio of intensity of these two peaks. It is interesting to note that

the peak at 1.88 eV excited with radiation at 436 nm becomes stronger with increasing current density than that for the shorter excitation wavelength. The luminescence spectra observed with different excitation wavelengths of 254 nm and 436 nm are compared in Fig. 4.7.

The typical photoluminescence spectrum of porous silicon at 300 K consist of a broad featureless band. The line shape of the PL band is frequently well described by a Gaussian distribution [149]. In some porous silicon samples, however, an additional structure in the luminescence spectrum was seen at temperatures below 80 K [159], [160], [161], [163]. The relative heights of the peaks of this fine structure seem to depend on processing conditions and post-preparation treatment [159]. In [163] and [162] the fine structure of the photoluminescence spectra was explained by a stepwise variation in the size-quantized elements of the porous silicon (by one silicon lattice constant), whereas the authors of [164] and [159] believe that this structure is related to the interference of the luminescence radiation in the porous silicon layer. In the latest model [165], the fine structure is interpreted as being due to the transitions between the electron vibrational levels inside the molecules formed on the PS surface. The PL reported by different researchers is centred in the orange-red spectral range [165]. One of the fine structure maxima lies at 1.88 eV, which corresponds to the maximum of our PL spectra. It is also interesting to note that the other groups [47], [174], [115], [166], [167], [56] have reported the existence of two bands in luminescence spectrum at room temperature. Maruyama et al. [47] have found that the peak wavelength (at 660 nm) changes continuously to shorter wavelength (at 600 nm) peak with extended exposure time by means that the peak at 600 nm becomes larger than the 660 nm peak. Pearsall et al. [174] reported that two overlapping emission bands exist in the orange-red region with the maxima just below 600 nm and around 680 nm. The short wavelength component is particularly intense immediately after excitation. Laiho et al. [115] have explained the red

Figure 4.8: PLE spectra of porous Si observed for two different emission bands of 620 nm and 660 nm for PS sample prepared with a current density of $76.6 \text{ mA} \cdot \text{cm}^{-2}$

shift of the spectrum with increase of time by the existence of two emission components with different lifetimes (the 590 nm band observed in a few μs and the 680 nm band observed within a few tens of μs). These two shoulders in luminescence can indicate the existence of more than one origin for the light emission. Thus, results of our spectroscopic measurements could be interpreted as luminescence due to overlapping of not less than two emission bands at $\approx 2.05 \text{ eV}$ (605 nm) and $\approx 1.88 \text{ eV}$ (660 nm).

We have also investigated the PLE spectra of our sample. Fig. 4.8 shows the PLE spectra of the sample 2d measured for the emission wavelength at 660 and 620 nm. We have not observed any differences in PLE spectra as a function of the emission wavelength in this range. This may indicate that in this range, the mechanism of the luminescence is the same. Unfortunately, we are not able to detect the PLE spectra for wavelengths λ_{PLE} larger than 600

nm because of an overlapping of the excitation wavelength and the emission band in this observed region.

4.4 Variation of Pt layer

Both Au and Pt are often used as a contact material in some optoelectronic devices. It is, therefore, necessary to study the influence of the evaporated Pt or Au layer on the properties of the PS films. Fig. 4.9 shows the PL

Figure 4.9: Normalized PL spectra of porous Si observed with excitation light of 254 nm for the sample 2a and the sample 2d with (b, d) or without a Pt film (a, c), respectively

spectra of the sample 2a with and without Pt layer and of the sample 2d.

The luminescence spectrum of "clean" sample 2a is, as can be seen in Fig. 4.9, structureless, with a single peak at ≈ 1.88 eV. Addition of a Pt layer to the sample reduces the PL intensity and alters this spectrum to one with two peaks, at ≈ 1.88 eV and 2.05 eV, respectively. It is interesting to note that the peak at 2.05 eV is also the maximum of the PL spectrum of sample 2d without Pt. For Pt-treated samples prepared at higher current density we have observed the quenching of PL spectra. The SEM images of surfaces of "Pt-coated" and "clean" PS are similar. Munder et al. [171] have studied the structure and luminescence properties of PS layers with an Au film on the surface. The Raman measurements have found no changes of the nanocrystal size distribution, thus indicating that the reduced PL intensity is not due to a change in the microscopic structure. As we know, the Pt adsorbs the light from 300 nm to 900 nm, i.e. exactly in the PS absorption (see chapter 6). This indicates, that the Pt-coated PS sample should absorb less light due to the high absorptivity of the Pt overlayer. This could explain the quenching of the whole PL spectrum of Pt-coated PS sample. We have, however, observed not only a quenching of the PL intensity, but a change in the ratio of intensities of two peaks at 1.88 eV and at 2.05 eV (Fig. 4.9 a, b) as well. If the Pt acts only as an attenuator, there should be no differences in the intensities of these two peaks. From that we conclude that some kind of interaction between our PS and Pt could exist. We can assume, that only a PS surface layer is coated with Pt. Thus, Pt is able to interact with luminescence centers in the surface. The peak at 1.88 eV is strongly quenched in contrast to that at 2.05 eV. This indicates that the emission band at 2.05 eV is due to luminescence centers existing in the surface (oxide) layer.

4.5 Gauss Deconvolution

In an attempt to understand better the mechanisms of luminescence, we have performed a Gaussian deconvolution of luminescence spectra of samples prepared with different current densities. Most of the investigated PS samples displayed bands of symmetric Gaussian shape, though some of them had a slight asymmetry with a broadening towards larger photon energy. The symmetric PL band shape was well described by the Gaussian distribution [149], [150]:

$$y(x) = \sum_{i=1}^n \frac{A_i}{w_i \cdot \sqrt{\frac{\pi}{2}}} \exp \frac{-2(x - x_{ci})^2}{w_i^2} + y_0 \quad (4.1)$$

An emission spectrum consists of a series of spectral lines, which can usually be represented by an analytical function containing three parameters for each line: position, height and width. A spectrum consisting of $n/3$ (with $n = 3, 6, \dots$) spectral lines thus requires n fit parameters. We initially deconvoluted our PL spectra of samples prepared with different current densities into two, three and four Gaussians without constraint of parameters. In table 4.1 we show for each of the PS samples the position of the luminescence peaks observed with excitation at 254 nm as a function of the number of Gaussians in the decomposition. For the deconvolution into two Gaussians, the position of the maxima is similar for all samples, except for sample 2a, where we observe a peak at 1.69 eV instead of 2.06 eV. This deviation (sample 2a) is due to uncertainty in the correction for apparatus response. For all our samples we found two peaks, the first at 2.06-2.01 eV and the second at 1.85-1.87 eV. Fig. 4.10 shows the two Gauss deconvolution of the PL spectrum of a sample 2e measured with excited radiation of 436 nm. Comparing these results with those of the deconvolution into three and four Gaussians, we have found that these two peaks, at $\approx 1.87 \text{ eV} \pm 0.03 \text{ eV}$ and $\approx 2.05 \text{ eV} \pm 0.03 \text{ eV}$, exist in the each deconvolution. The decomposition into four

Sample	J_A [mA · cm ⁻²]	Peak	2 Gaussians	3 Gaussians	4 Gaussians
2a	25.5	1		2.067 eV	2.04 eV
		2			1.98 eV
		3	1.87 eV	1.87 eV	1.86 eV
		4	1.69 eV	1.70 eV	1.72 eV
2b	51	1	2.06 eV	2.05 eV	2.08 eV
		2			2.00 eV
		3		1.89 eV	1.88 eV
		4	1.88 eV	1.86 eV	1.87 eV
2c	76.5	1	2.01 eV	2.09 eV	2.07 eV
		2			1.99 eV
		3		1.84 eV	1.98 eV
		4	1.86 eV	1.87 eV	1.86 eV
2d	102	1	2.03 eV	2.04 eV	2.08 eV
		2			2.0 eV
		3		1.84 eV	1.89 eV
		4	1.83 eV	1.87 eV	1.87 eV
2e	127.5	1	2.06 eV	2.11 eV	2.09 eV
		2		2.01 eV	2.00 eV
		3		1.92 eV	1.91 eV
		4	1.85 eV		1.87 eV

Table 4.1: The position of each peak for the deconvolution into two, three, four Gaussians of PL spectra.

Figure 4.10: Deconvolution of PL spectrum into two Gaussians of sample 2e measured with excitation radiation of 436 nm.

Gaussians could be written as the sum of these two peaks and two other additional curves ranging between ≈ 1.7 eV and ≈ 1.99 eV. The increase of number of Gaussians causes only a decrease of the standard deviation. The existence of two Gauss curves with similar position of the maximum at each deconvolution could suggest that the deconvolution for our luminescence spectra is natural and should reflect some underlying essential physics. In the chapter 4.3.2, we have observed for our samples (Fig. 4.6) systematic dependencies for the ratio of intensities of two peaks at ≈ 2.05 eV and at ≈ 1.87 eV for different current density.

The intensity of the band at ≈ 2.05 eV increases with a simultaneous de-

Sample	2a	2b	2c	2d	2e
Gaussian1	1	1	1.3	4.2	5.72
Gaussian2	3.85	1.53	1	1	1

Table 4.2: The ratio of the relative intensities of two Gaussians at ≈ 2.05 eV and at ≈ 1.87 eV for different J_A

crease of the peak at ≈ 1.87 eV for a higher current density. The similar behaviour for the Gaussians of our fit (table 4.2) could be observed. We have also found the similar evolution of intensities of both Gauss curves to our measured luminescence spectra (Fig. 4.7) for a different excitation wavelength. Fig. 4.11 shows the measured and four Gaussian fitted PL spectra of sample 2c for excited light of wavelength 245 nm and 436 nm, respectively. In the former case, we have observed that the ratio of the intensities of the peaks at ≈ 2.05 and ≈ 1.88 is 1.3 :1, whereas in the latter this is 1:1.47. This confirms our assumption that our photoluminescence spectra consist of at least two overlapping emission bands. Depending on the peak intensity ratio, experimental spectra can resemble a single-peak or double-peak curve. The behaviour suggests that luminescence originates from possibly two different types of radiative recombination centers localized in energy. Radiative recombination occurs when electron-hole pairs created by interband transition are trapped and localized during the local lattice distortion. Due to the lattice deformation around the luminescence center, the spectra have the Gaussian-like shape with the large halfwidth [113] also observed in our experiments. In the case of peak 1, we have observed with increasing current density not only a continuous increase in FWHM but also in the relative areas as well. Conversely for peak 2 we have found a decrease in the FWHM

Figure 4.11: Comparison of experimental data with fitting (four Gaussians) for PL spectra of sample 2c observed at excitation radiation of 254 nm and of 436 nm. Dotted curve designates the experimental data (upper part). Standard deviation of fitting to experimental data measured at 254 nm (dotted line) and at 436 nm (solid line) (lower part)

Sample	Current Density [mA · cm ⁻²]	Peak1		Peak2	
		FWHM	Area	FWHM	Area
2a	25.5	46.5	64.9	10	52
2b	51.0	55.6	33.1	34.4	10.6
2c	76.5	63	32.3	45.1	8.5
2d	102.0	60.9	24	50.5	2.7
2e	127.5	63.4	21.2	69.5	4

Table 4.3: The FWHM and the area of single Gauss band for different current densities

and in the area for higher current density (table 4.3). These behaviours suggest the radiative recombination through localized luminescence centers. Furthermore, we have also performed the deconvolution of our spectra for different HF concentration and we have found these two emission bands: at ≈ 1.88 eV and slightly shifted at ≈ 2.09 eV.

Based on our results we can conclude that luminescence is due to at least two different types of luminescence centers.

4.6 Discussion and Summary

The room-temperature photoluminescence and structure of porous silicon samples obtained at various etching conditions (variation of current densities and of HF concentration) were studied. We have observed in our samples the increase of thickness of the porous layer and density of pores for a higher HF concentration. There is, however, no visible difference either in the cross-section SEM images in thickness or in the microstructure (SEM,

STM images) of surface layers of PS samples prepared at various current densities. Further, the evolution of the PL spectrum from a single peak at ~ 1.88 eV into two peaks at ~ 1.88 eV and ~ 2.05 eV for higher current density (Fig. 4.6 and 4.7) could be observed.

The behaviour is used to be explained as the blueshift of PL spectra. We would rather explain it as enhancement of the short-wavelengths and the quenching of the lonwavelengths. This means that the individual components, in our case at least two, can be selectively enhanced or decreased. This assumption could confirm our further results. We have found systematic dependencies in the ratio of intensities of the two PL bands on the current density and on the excitation wavelength. Their position does not, however, change on varying etching parameters. The behaviour of PL spectra suggest, that luminescence originates from possibly two different luminescence centers. Further, we have studied the PL behaviour of PS sample coated with a Pt layer. We have observed the quenching of PL spectra as well the change in the intensities of two peaks (1.88 eV and 2.05 eV). Because, the PS surface layer absorbs from 300 nm to 900 nm, there should be no differences of these two peaks. From that, we conclude that some kind of interaction between our PS ant Pt could exist. Assuming that the PS surface layer is mainly coated with Pt, we can say that Pt is able to interact with luminescence centers in the PS surface. The peak at 2.05 eV is less quenched than that of 1.88 eV. This indicate that the emission band at 2.05 eV is due to luminescence centers existing in the surface (oxide) layer.

In order to explain and to confirm the two-band behaviour of our PL spectra, we have analyzed them by the deconvolution into two, three and four Gaussians. We have found that our spectra can be well fitted as the sum of two Gaussians at ~ 1.87 eV and at ~ 2.05 eV. It is interesting to note that the position of each Gaussian changes weakly with different preparation parameters. Furthermore, these two Gaussians at ~ 1.87 eV and at ~ 2.05 eV

exist in each deconvolution. The increasing number of Gaussians decreases only the standard deviation. We have observed also systematic dependencies in the area and the relative FWHM with changing of current density and a HF concentration. These results confirm our assumption that the individual components can be selectively enhanced or decreased.

The involvement of defects, similar to a nonbridging oxygen hole center in silica fibers, has recently been proposed to explain the red luminescence in porous silicon [139]. It was suggested that these centers are located at the silicon-oxide interface. It is well known that an emission band is observed in SiO_2 at 1.9 eV (corresponding to wavelengths of 650) [168], [116] and [169], which co-incides with an emission band in PS. The time constant for the 1.9 eV (650 nm) emission band in SiO_2 assigned to the non-bridging oxygen hole center, is 10-15 μs at room temperature [168] which is very close to that reported by Vial et al. [54] for 650 nm emission from porous silicon. This band is very close, if we take in the account the accuracy (1 nm) of our measurements, to the band observed in our samples. The band at 1.88 has also been found to be one of the energy position of the fine structure [149]. Further, as has been mentioned above, the peak has been observed to occur after an exposure the PS samples to ambient air. Its intensity increases slowly in its initial stage but the increase is accelerated with extending exposure time [47]. As we know from chapter 2.3, during ambient exposure, this Si-H on the surface of H passivated surface of the Si clusters is gradually replaced by an oxide [27]. This indicate that the peak at ~ 1.88 eV is related luminescence centres lying in the oxide layers or in the interface SiO_2 /nanoscale silicon. Conversely, based on results, particulary on PL measurements of PS sample with and without Pt overlayer, we can conclude that the second PL band at ~ 2.05 eV is due to luminescence centers located on the surface (oxide) layer. Our results strongly support the QCLC proposed by Qin and Jia [137].

Chapter 5

Spectroscopic and SXM Investigations of Porous Silicon Doped with Dyes

Organic dyes have been widely used for many years in frequency-tunable lasing structures [224]. Although they have found use first of all in the liquid phase, there is growing interest in incorporating laser dyes into solid state media for device applications. On the other hand, any opportunities to tune optical properties of a PS material are of great interest. A combination of such materials could be applied for the development of new materials for quantum electronics, nonlinear optics and solar-energy devices [225].

Canham [226] has reported on properties of PS doped with various laser dyes focusing on properties of the impregnated dyes. We have developed an alternative approach i.e. studying an influence of PS doping with dyes on optical and structural properties of the PS layers themselves [227]. The purpose of this chapter is to extend this approach to the dopants which absorb and emit light in different spectral regions (Stilbene 1, Coumarine 153, Rhodamine 110, and Kiton Red) in order to control emission wavelength

of the PS layers.

5.1 Description of samples

5.1.1 Rhodamine 110

The PS layers have been formed by anodization of the wafers ((100) p-type (boron-doped) Si with resistivity of $1 \Omega \cdot cm$) in a HF (40%) + C_2H_5OH (1:1) electrolyte. During anodization for 2 and 10 min the current density was kept constant at 3 or $1.7 mA \cdot cm^{-2}$ for samples A and B, respectively. The samples were then exposed to ambient air for 10 days and cut into pieces.

Figure 5.1: The chemical structure of Rhodamine 110

One piece of each sample was doped with Rh110 [213] by soaking it in an ethanol solution containing a concentration of $3.3 \cdot 10^{-3}$ M of Rh110 (Fig. 5.1).

5.1.2 Kiton Red and Stilbene1

The investigations were performed on PS layers formed by anodization of the wafers ((100) p-type (boron-doped) Si with the resistivity of $10 \Omega \cdot cm$) in a HF (40% wt.) + C_2H_5OH (1:1) electrolyte at constant current density ($3.2 mA \cdot cm^{-2}$) for 2 minutes.

The PS films produced were about $1.6 \mu m$ thick and emitted red light. The samples were doped with laser dyes by soaking them in an ethanolic solution,

Figure 5.2: The chemical structure of Stilbene 1 (St1)

sample C: of Stilbene 1 $1.6 \cdot 10^{-3}$ M (Fig. 5.2) and sample D: of Kiton Red 620 $1.5 \cdot 10^{-3}$ M (Fig. 5.3) [213] using two different techniques (Fig. 5.4). In the first, the freshly etched samples (samples 1C and 1D) were immersed in the dye solutions (St1 and Kt, respectively) just after rinsing with absolute ethanol (Fig. 5.4 a).

After immersion of the samples into solution we have observed bubbling on the PS layer surface. In our opinion the observed bubbling indicates that dye

Figure 5.3: The chemical structure of Kiton Red 620 (Kt)

molecules are involved in a chemical reaction with the active surface of PS since an immersion of the same samples into pure ethanol does not produce any evidences of a chemical reaction. In the second technique (Fig. 5.4b) the samples (2C, 2D) are initially aged (48 hours) and then the process described

Figure 5.4: Idealized cross-sectional schematic view showing dye impregnation in PS samples (a) when freshly etched (b) when aged.

above is carried out. In this case we have not observed any manifestations of chemical reactions.

5.1.3 Coumarine 153

The PS layers (sample E) were formed by the anodization of p-type (100) Si wafer (resistivity of $10 \Omega \cdot \text{cm}$) at the constant current 21.6 mA in the solution of HF (40% wt.): H_2O : NaNO_2 (50:50:1) for 10 minutes. After 5 days exposure to the air, the sample (sample E) was doped with Coumarine 153 (Cou153 [213]) by immersion into an ethanol solution containing a concentration of $3.3 \cdot 10^{-3}$ M of Coumarine 153 (Fig. 5.5). After the doping and drying (30 min, room temperature on air), the surfaces of all samples were rinsed with ethanol to remove the precipitated dyes. The samples were then exposed to air before PL and SEM measurements were carried out. PL spectra of the samples were measured with a Shimadzu RF-5001 PC spectrofluorophotometer at room temperature. The spectra were corrected for the apparatus response. The concentration of the dyes in the solutions has been determined by their visible absorption measured with a Shimadzu

Figure 5.5: The chemical structure of Coumarine 153

UV240 spectrophotometer. The porosity of the samples has been measured using the method of ultrasonic surface wavelengths [214]. The surface structure and cross section of the PS layers was investigated using a SEM Philips 515 operated at 30 keV in energy and with a current density of $3A \cdot cm^{-2}$ at room temperature.

5.2 Results and Discussion

5.2.1 Rhodamine 110

Structure and Photoluminescence of PS

The longer time of the anodization and lower current density for sample B in comparison with sample A results in the formation of a thicker layer of PS with a finer structure (see Fig. 5.6) and higher porosity. For sample A the PS layer is ≈ 300 nm thick and the characteristic surface features of the PS structures ranges from 50 to 75 nm (porosity is 20 %), whereas in sample B these parameters are ≈ 600 nm and 25-50 nm (porosity of >50 %), respectively.

According to the well-known model of the elementary structure of a PS layer

Figure 5.6: Cross-sectional SEM micrographs of the PS samples, (sample A and sample B)

(see e. g. [92]), it consists of small Si crystallites coated with an inhomogeneous layer of silicon-backbone (siloxene, amorphous silicon, silicon oxides etc.) compounds [225], (see chapter 2). Generally, this structure has two interfaces (between the crystallite C and layer L (interface 1), and the interface of layer L with air containing numerous defects of various origins.

PL spectra of the samples excited at 250 nm are shown in Fig. 5.8. As seen from Fig 5.8, the PL band of sample B (in the range of 600-800 nm) is

Figure 5.7: The schematic description of porous structure. Interface 1 (1) between the crystallite C and layer L and the interface 2 (2) between the layer L and air.

(interface 2) (see Fig. 5.7) shifted to the red by 30 nm compared to that of sample A (Fig. 5.8). According to [215], [101], [216] and the results described in the chapter 5, PS emission in the range of 600-800 nm is likely to be due to emission of defects in layer L and on the interfaces 1 and 2. Therefore, the red shift of the PL band in sample B with respect to that of sample

Figure 5.8: The room temperature normalized photoluminescence spectra of porous silicon measured with excitation at 250 nm.

A is most probably caused by the change in ratio of PL emitted by the defects of interface 2 and layer L (Fig. 5.8) due to the different values of the sample porosity. For sample B, the relative intensity of the interface 2 defects should be higher due to a higher specific surface of the PS layer with higher porosity. Simple model calculations show the considerably higher (by a factor of 5) specific surface for sample B compared to that of sample A. On the other hand, the PL from the layer 2 is rather sensitive to chemical modification [101]. Thus, effects due to the change in effective ligation of the surface Si layers with the time of etching might also contribute to the

Figure 5.9: PL spectra (normalized for intensity of red band) of sample A before and after doping with laser dyes Rh110 measured with an excitation wavelength of 436 nm.

observed behaviour of the red PL band.

Upon excitation at 436 nm one also observes a blue-green PL band (Fig. 5.9, Fig. 5.10). This part of PS emission may be attributed to excitons formed within crystallites [217] and to defects at interface 1 and in layer 2 [215], [216]. The relative intensity of this band with respect to the red PL is higher for sample A as compared to that for sample B (Fig. 5.8, Fig. 5.9). This difference may be due to additional red emission attributed to the interface 2 defects in sample B.

PL of PS doped with Rhodamine 110

First of all it should be mentioned that soaking the samples with pure ethanol has no effect on the PL measured after drying compared to that measured before soaking. Conversely, hand soaking the samples with a Rh110 solution

Figure 5.10: Normalized PL spectra (normalized for intensity of red band) of sample B before and after doping with laser dyes Rh110 measured with an excitation wavelength of 436 nm

in ethanol has a drastic effect on the PS PL spectra. The PL of the PS samples doped with Rh110 is strongly quenched so that the peak intensity of the red PL is reduced by a factor of ≈ 30 and the blue-green PL is not detected in the cw spectra (Fig. 5.9, Fig. 5.10). At the same time, the shape of the red band in the doped sample B changes upon the dye impregnation so that its peak is shifted to the blue (Fig. 5.10). For sample A the shape of the red PL band remains practically the same except for a slight broadening upon the dye impregnation (Fig. 5.9). These effects take place due to the different quenching of the short- and long-wave parts of the red PS PL band and are discussed in more details below. No substantial emission from the dopant except the minor peak at ≈ 540 nm (compare with the peak of Rh110 in ethanol at 535 nm [213]) in sample B (Fig. 5.10) and the hardly detectable

peak in sample A (Fig. 5.9) is observed. The difference between these samples may be explained by their different porosity and correspondingly the higher concentration of Rh110 adsorbed on the walls of pores in sample B. The absence of substantial emission of Rh110 impregnated into PS is in good agreement with results obtained by Canham for similarly prepared samples [226].

Laser dyes are well known to have large absorption coefficients in their principal band, e.g. Rh110 has a decimal extinction coefficient of $8.99 \cdot 10^4 M^{-1} \cdot cm^{-1}$ [213]. On the other hand, as shown previously in [230], [233] absorption spectra of the dye molecules adsorbed in a porous matrix are not affected to any great extent. When intermolecular distances and resonance conditions are appropriate, the dipolar absorption transition of Rh110 molecules interacts with emitting dipoles through dipole-dipole interaction, i.e. via excitonic coupling [218] or non-radiative excitation energy transfer (ET) [219]. As mentioned above, the blue-green emission of PS is due to emission of the defects in layer 2 or at interface 1 [208], [216]. The blue-green emission is dipolar since the degree of PL polarization is up to 40% [220] when the PL is excited into emissive transition. Furthermore, this emission has a very large spectral overlap with absorption of the Rh110 molecules adsorbed on interface 2 (see Fig. 5.10) and long lifetime (effective lifetime of $< 2 \mu s$ [221]). However, we do not know whether the distances between adsorbed Rh110 molecules and the emitting entities are covered by the range appropriate for an effective ET. Taking into account characteristic distances calculated for non-radiative ET in supramolecular systems [222], one can conclude that the distance between the emitting entity in the PS and the adsorbed dye molecules should not exceed ≈ 5 nm in order to facilitate an effective intermolecular ET. The thickness of layer L might be in this order of magnitude since the native oxide layer formed on a surface of crystalline silicon at room temperature is thinner than 5 nm [223]. Thus, the quenching of the green-

blue emission of PS may be attributed to an effective ET from the defects in layer 2 and at interface 1 to the Rh110 molecules. The excitations in the dye molecules undergo a non-radiative deactivation process probably due to fast electron transfer to the pore material [226].

The change in the shape of the red PL band in sample B upon doping may be explained by the interaction of the adsorbed dye molecules with the defects of interface 2 which will be more effective than the corresponding interaction with the defects in layer L due to localization of the molecules on the pore surface. The difference in behavior of the band shape for the different samples is explained by the higher concentration of surface defects in sample B due to its higher porosity as has already been discussed before.

In order to prove the proposed mechanism we have performed the PL study of PS samples doped with dyes absorbing in other spectral ranges.

5.2.2 Kiton Red and Stilbene1

Structural features

Fig. 5.11 shows microstructures of the PS layers impregnated with St1 using the two different techniques mentioned above (Fig. 5.4). Pores with diameter ranging from 25 to 50 nm are clearly observed on the surface of the PS layer doped with St1 just after preparation (sample 1C). In contrast, a porous structure of the PS layer doped after aging (sample 2C) could not be resolved. Similar effects are observed for the PS samples impregnated with Kt before and after aging. According to [228], the skeleton surface of freshly etched PS is covered with Si hydride layer (see chapter 2) while that of the aged PS layers is oxidized [28]. This provides a clue to the interpretation of the mentioned differences in the behaviour of freshly etched and aged samples during the doping. A Si hydride surface is chemically more active due to dangling bonds [229] in comparison to the oxidized Si one. Thus, it can

Figure 5.11: SEM images of the PS layers impregnated with Stilbene 1 using two different techniques mentioned in the chapter 6.1.2.

be understood why a chemical reaction is observed in sample 1C with dye molecules adsorbed on the pore surface whereas in the sample 2C does not. The reaction probably causes an additional etching of the PS layer, thus increasing the pore diameters as observed on the microphotographs (Fig. 5.11).

Photoluminescence effects

PL spectra of the samples are shown in Fig. 5.12. As seen from the figure the PS layers doped with the same dye before and after aging (e.g. samples 1C and 2C, respectively) emit approximately in the same region (1.7-2.3 eV). This observation leads us to a conclusion that the PL properties of the doped PS layer are insensitive to the method of dye impregnation as well as to the presence of chemical reactions involving dye molecules. The variation of PS luminescence properties is likely to be due to adsorption of the dye molecules on the pore surface. Such an adsorption might modify the luminescent defects existing on the PS pore surface [28] or lead to physical processes involving dye molecules (e. g. energy transfer from the luminescent sites to the ad-

Figure 5.12: Normalized PL spectra of the samples doped with laser dyes (sample 1C, 2C with Stilbene 1 and sample 1D, 2D with Kiton Red)

sorbed dye molecules). A situation, where PS doped with a dye before and after aging emitting almost in the same region, is possible if the chemical or physical processes remain essentially the same. In our case this means that either luminescence sites modified after a dye impregnation are the same for the freshly etched and aged samples or conditions under which the photo-physical processes take place in such samples are essentially unchanged. On the other hand, emission energies of the samples prepared by the same technique using different dyes (e.g. samples 1C and 1D) are different (1.7-2.3 eV E_{max} =2.0 eV and 1.6-2.2 eV E_{max} =1.8 eV, respectively) with practically the same emission bandwidths ($\Delta E_{1/2}$ =0.6 eV for samples 1C and 1D). Hence, the PL band peak of the Kt doped samples (e.g. sample 1D) is shifted to the red (ΔE =0.3 eV) compared to that of the St1 doped samples (e.g. sample 1C). Whether this difference is caused by different spectral properties of St1

and Kt molecules or their different chemical structures cannot at present be solved. Finally, PL bands of the PS samples doped with the dyes before and after aging show some minor differences. Hence, the PL band of sample 1C is narrower by 0.2 eV compared to that of sample 2C ($\Delta E_{1/2}=0.8$ eV), due to additional emission in the range from 2.0 to 1.7 eV. At the same time, for the sample impregnated with Kt after aging (sample 2D) the whole PL band is shifted to the blue by about 40 meV, with an increase in the relative intensity of its blue part compared to that of the sample doped before aging (sample 1D). This situation is similar to that of the PL spectra of the aged samples doped with St1 and Kt (2C and 2D), which are closer to each other in comparison with those of the samples doped before aging (1C and 1D). Such a spectral behaviour could be possible when processes leading to modification of PL spectra of the samples doped with the dyes are less efficient for the aged, i.e. partly oxidized, PS layers.

At present it is hard to identify the real nature of the processes leading to modification of the PS luminescence upon a dye impregnation. To solve this problem both the chemical (experiments with compounds containing groups analogous to those of the investigated dyes) and physical (time-resolved spectroscopy) methods will be used in chapter 6.2.3.

5.2.3 Coumarine 153

Fig. 5.13 shows PL spectra of sample E, when undoped and when doped with Cou153, observed at the excitation wavelength of 254 nm. As seen from Fig. 5.13, the PL band of sample E consists of two peaks at 1.86 eV (665 nm) and at 2.0 eV (619 nm). This two-peak PL spectrum could indicate the existence of at least two emission bands, as described in the chapter 4.

To understand their nature we have also investigated the PLE spectra of our samples. Fig. 5.14 shows the PLE spectra of the sample C measured for the

Figure 5.13: Normalized PL spectra (normalized for intensity of the band at 2.0 eV) of sample 1E before (solid line) and after doping (dotted line) with the laser dye Cou153 measured at an excitation wavelength of 254 nm

emission wavelength at 720 nm and 665 nm. Both excitation spectra have different structure. For the emission at 720 nm the peak at 2.86 eV (433 nm) is higher than that at 3.15 eV (394 nm). Conversely, we observed opposite behaviour for the emission at 665 nm. This suggests that the luminescence comes from two different types of luminescence centers, as mentioned in the chapter 4.

It is important to note, that we are only able to correct the spectra from 300 nm to 850 nm. Because of that and the low detection sensitivity of the spectrofluorometer below 300 nm, the PLE measurements in the range of wavelengths below 300 nm are not reliable. After Cou153 doping of sample E, we have observed a quenching of the PL spectrum and a change in the ratio of the intensity of these two peaks (Fig. 5.13). The peak at 1.86 eV,

Figure 5.14: Normalized PLE spectra of sample 1E measured at an emission wavelength of 720 nm and of 665 nm

however, is strongly quenched in contrast to that at 2.0 eV, which remains unaltered, except for a slight blue shift of 0.03 eV (9 nm).

Fig. 5.15 shows the PLE (upper part) for the Cou153 doped sample E at an emission wavelength of 530 nm and the absorption spectrum (lower part) of Coumarine 153 dissolved in ethanol. As we can see in Fig. 5.14 (lower part), Cou153 absorbs mainly in three spectral regions, from 200 nm to 240 nm (5.7 eV \simeq 218 nm maximum), from 245 nm to 310 nm (4.9 eV \simeq 266 nm maximum) and 340 nm to 510 nm with the maximum at 2.93 eV (423 nm), i.e. exactly in the PS absorption range (Fig. 5.15 upper part). This indicates that the PS sample doped with Cou153 should absorb less light due to the high factor of absorptivity of the dye molecules in the mentioned wavelength region in comparison to the undoped PS sample. This could explain the quenching of the whole PL spectrum of the Coum153 doped

sample 1E, excited at 254 nm. Based on these results, we can thus say, that the Cou153 acts as an attenuator. We have, however, observed not

Figure 5.15: Normalized PLE spectra of sample E after doping with Cou153 measured at an emission wavelength of 530 nm (upper part) and the absorption spectrum of Coumarine 153 dissolved in ethanol (lower part)

only the a quenching of the PL intensity of sample 1E after Cou153 doping, but a change in the ratio of the intensity of the two peaks at 1.86 eV (665 nm) and at 2.0 eV (619 nm). If the Cou153 acts only as an attenuator there should be no differences in the intensities of these two peaks. From

Figure 5.16: Normalized PL spectra (normalized for intensity of the red band) of sample 1E before and after doping with the laser dye Cou153 measured at an excitation wavelength of 436 nm

that we conclude, that some kind of interaction between our PS and Cou153 could exist. We can assume that Cou153 is adsorbed on the surface layer of PS sample. Because of that, Cou153 is only able to interact with the luminescence centers on the surface. This indicates, that the emission band at 2 eV is due to the luminescence centers existing in the surface (oxide) layer. For the excitation at 436 nm, however, we have observed not only quenching of the PL spectrum of sample E upon dye impregnation, but a significant blue shift of 30 nm (Fig. 5.16) as well. The PL of both the Cou153 doped and undoped sample E is a typical single-peak spectrum at 1.75 eV (708 nm) (undoped PS sample) and at 1.83 eV (678 nm) (PS sample doped with Cou153). Fig. 5.17 shows the excitation spectra for the undoped and Cou153 doped sample E at the emission wavelength of 665 nm. One can recognize a

Figure 5.17: Normalized PLE spectra of sample E before and after doping with the laser dye Cou153 measured at emission wavelength of 665 nm

change in the ratio of the two peaks (at 1.75 eV and at 1.83 eV) with respect to both samples. This is due to the fact, that the light intensity that excites the PS is now modulated by the absorption of Coum153 (Fig. 5.14 lower part). This means that Coum153 acts as a filter for the incident light and so modifies the luminescence distribution. This could explain a shift of the PL spectra of the PS sample after Cou153 doping, but as we believe not as large as we have observed (≈ 30 nm Fig. 5.16). That is why we think, that there must be some kind of interaction between the Cou153 and porous silicon. The peak at 2.0 eV observed at the excitation wavelength of 254 nm (Fig. 5.13) could not be resolved. This may be explained by a resonant excitation of undoped PS sample (Fig. 5.14) at the absorption band at 433 nm. This means that the strong luminescence band at 1.86 eV covers this band due to its lower intensity. We have observed, however, a substantial emission from

Figure 5.18: Fluorescence decay of Coumarine 153 in PS sample :experimental data (dotted line) and fit (solid line) measured at 530 nm

the dopant at ≈ 2.43 eV (Fig. 5.16). We have not found a peak of Cou153 in the PL spectrum of the doped sample measured at the excitation light of 254 nm, due to the existence of the second order of excitation light coming from a monochromator. Based on these results, particularly on the blue shift of PL spectra after doping with Cou153, we can say, that some kind of interaction between the dye molecule and PS sample might take place.

Fig. 5.18 shows the time resolved fluorescence (TRF) of Cou153 in the PS sample E and the fit to measured data. The half-logarithmic representation of our experimental data indicates no simple exponential behaviour of a TRF. Similar behaviour of PL decay profiles of Rhodamine B in a porous glass has been reported by Even et al.[234]. Based on [234] we have fitted our data with a stretched exponential decay function given by:

$$F(t) = A \exp - \left(\frac{t}{\tau_1}\right)^\beta \exp\left[-\left(\frac{t}{\tau_0}\right)\right] + B \exp\left[-\left(\frac{t}{\tau_2}\right)\right] \quad (5.1)$$

The $B \exp\left[-\left(\frac{t}{\tau_2}\right)\right]$ term represents the part of fluorescence decays in the mea-

surement data with a decay time in the range of the system response and the $A \exp - (\frac{t}{\tau_1})^\beta \exp - (\frac{t}{\tau_0})$ describes the fluorescence decay, in which τ_0 represents the intrinsic lifetime of the material, in our case of Coumarine 153. The value of τ_0 has been fixed to 10 ns during the fitting procedure, which corresponds to the lifetime of Cou153 dissolved in ethanol. As we can see from Fig. 5.18, the experimental data is well fitted by the function (5.1). The most important parameters are τ_1 and β . The coefficient β describes the distribution of $(decayrates)^{-1}$ of the molecules and ranges in value from 0 to 1. For $\beta=1$ the fitted function is a normal exponential function. In our case, β is 0.26 (Fig. 5.18), which is indicative for a nonexponential behaviour of the decay. Parameter τ_1 represents the mean lifetime of the molecules in the environment specific to the experiment in question. The value of τ_1 of 0.09 ns shows that the PL of Coumarine 153 in our PS sample decays considerably faster than in the pure Coumarine solution. It can be inferred that some sort of interaction (e.g. energy transfer) between Cou153 and the PS occurs in our doped PS samples or a reabsorption process of the Coumarine 153 takes place.

Based on these results and those described above, we can say that Coumarine 153 not only acts as a filter for the absorption of the PS sample but interacts with the PS samples as well, resulting in a change of the optical properties of our sample.

5.3 Summary

We have investigated changes in the structure and the luminescence properties of porous silicon samples to that samples doped with laser dyes like Rhodamine 110, Kiton Red, Stilbene 1 and Coumarine 153. We have found for all examined PS samples quenching and a shift of the photoluminescence upon dye impregnation. Our results show, that the quenching of the PL

intensity is due to the absorbitivity of the laser dyes. We have, however, measured a change in the ratio of the intensity of two PL peaks at 1.86 eV and 2.0 eV observed (at excitation wavelength of 254 nm) for undoped PS samples after doping with dyes (Cou153) and a shift of the PL spectrum (at excitation wavelength of 436 nm) as well. This two-peak behaviour indicates, that some kind of interaction between our PS and Cou153 could exist. The peak at 1.86 eV is strongly quenched in contrast to that at 2.0 eV. Because Cou153 is adsorbed on the surface layer of the PS sample, it is only able to interact with luminescence centers on the surface. From this we conclude that the emission band at 2.0 eV is due to luminescence centers existing in the surface(oxide) layer. Based on these results and on the blue shift of the PL spectra after Cou153 doping, we can say that an interaction (e.g. electron transfer) between the molecule and PS sample occurs in our doped PS samples. TRF measurements also confirm this assumption. They do not, however, exclude a reabsorption processes in the Coumarine 153. The results obtained could be helpful in terms of tuning the photoluminescence range of porous silicon.

Chapter 6

”Writing” of Optical Patterns on Porous Silicon by an Electron Beam

Most patterning techniques rely on high resolution electron beam lithography performed with scanning electron beam systems. The challenges ahead lie in the degree of lateral control in which the lithography by charged particle beams can be performed, i.e. resolution and placement accuracy. Barbour et al. [248] reported that the light-emitting porous Si was patterned by eliminating luminescence by ion irradiation. Batstone et al. [242] have shown that PL activity can be patterned by high-energy electron bombardment.

In this chapter, we report on the first efforts towards localized luminescence patterning of porous silicon on a micrometer scale using an electron beam as a lithographic tool. Recently, cathodoluminescence of porous silicon (see chapter 2.4.3) has been reported [72], [78], [42], [79], [238], but the studies have been concentrated on the properties and behaviour of the technique itself. It has been shown that simultaneous measurements of the light emission (photon mapping) and surface topography reveal changes in photon emission

intensity on the porous structure due to sample inhomogenities as well as due to sample deterioration by the electron beam.

In our approach we have concentrated the attention not on finding an explanation for the CL mechanism in porous silicon, but on the use of this technique to show the possibility of fabrication of well-defined optical patterns on a micrometer scale in PS layers. Furthermore, we have investigated the cathodo- and photoluminescence and structural properties of these patterns on PS layers at two different temperatures (at room temperature and at 77 K).

6.1 Description of samples and instrumentalions

The investigations were performed on an electrochemically etched p-type (Boron-doped) Si wafer (100), resistivity of $10 \Omega \cdot \text{cm}$ in HF (40% wt.) + $\text{C}_2\text{H}_5\text{OH}$ + NaNO_2 (50:50:1) electrolyte. The anodization lasted 2 minutes, during which time the current density was kept at $8,4 \text{ mA} \cdot \text{cm}^{-2}$. The samples were exposed to the air for one day (sample A) and for approximately one year (sample B) before CL and SEM measurements.

The cathodoluminescence (CL) mappings were taken by a modified commercial scanning electron microscope (SEM) Philips SEM 515 at room temperature. The CL system is able to detect radiation from 350 nm to 700 nm (see chapter 3.3.2 for the detailed description of the whole system).

The spectroscopic measurements of the cathodoluminescence of the PS samples were taken with SEM CamScan CS 44 at the University Leipzig operated at 10 keV in energy and with a current of 800 pA. The system is able to detect radiation from 350 nm to 800 nm with a 0.5 nm resolution. The CL spectrum was measured starting from the short-wavelength limit and the time of the

measurement of each point was 4 ms.

PL spectra of the samples were measured with a Shimadzu RF-5001 PC spectrofluorophotometer at room temperature, and the spectra were corrected for the apparatus response. The surface structure and a cross-section of the PS layers were investigated by a scanning electron microscope (SEM Philips 515) operated at 30 keV in energy and with a current density of $0.3 \text{ A} \cdot \text{cm}^{-2}$ at room temperature. For this purpose, we have sputtered a Pt film, approximately 5 nm thick onto the surface layer of the sample by a DC-diode sputtering system according to [121].

6.2 Results and Discussion

6.2.1 Structure and Luminescence

The cathodoluminescence as well as the surface microstructure of the PS layers are spatially inhomogenous. In CL, one observes dark circular patches

Figure 6.1: SEM images of the surface morphology of a PS sample. We can see the difference in the roughness of the PS layers (a) structure 1 and (b) structure 2 of the sample B.

which probably originate from gas bubbles staying on the surface during

Figure 6.2: Cross-sectional SEM image of the porous sample

the etching process. The SEM image of the structure of the PS sample is shown in Fig. 6.1. We have observed two kinds of porous structure. The first, (structure 1), is highly strained and porous (dark circular patches in CL (Fig. 6.6). The pores with diameters ranging from 25 to 50 nm are clearly observed on the surface of the PS layer (Fig. 6.1 a). The second, (structure 2), is less porous and its surface structure could not be so well resolved as the first (Fig. 6.1 b). However, we have not observed any significant differences for both structures in the thickness (about 1.8 μm) as well as in the microstructure in the cross section SEM image (Fig. 6.2). Each layer has a porous structure, as commonly reported in the literature [156]. However, the differences in the structure can also be seen in the photoluminescence spectra and cathodoluminescence images. It is interesting to note that the dark circular regions (structure 1) seen in the SEM image (Fig. 6.1) are also dark in the photoluminescence (Fig. 6.7) and CL image (Fig. 6.6). In contrast, a PL and CL of the PS structure 2 shows a bright luminescence. Fig. 6.3 shows the PL spectra of structure 2 sample A. The PL spectrum exhibits a peak with an FWHM of 0.39 eV at 1.90 eV (650 nm) and at 1.85 eV (670 nm) for the excitation energies of 254 nm and of 300 nm, respectively. These are typical PL spectra of porous silicon layers as reported in the literature

Figure 6.3: PL spectra of the same porous Si sample observed with two different excitation wavelengths of 254 nm and of 300 nm

[189].

Furthermore, we have performed the spectroscopic CL measurements at room temperature and at 77 K. Unfortunately, we have not been able to record the CL spectrum at room temperature due to rapid quenching of the intensity of the emission band during the measurement. However, we have measured the cathodoluminescence spectrum (Fig. 6.4) of our sample at 77 K. It consists of two peaks: a relatively large and broad emission band at ≈ 2 eV and a small peak at ≈ 2.67 eV for structure 2. It is interesting to note that the luminescence of structure 1 consists only of a single peak at ≈ 2.67 eV at 77 K. The CL band at 2 eV could correspond to the peak observed at 1.9 eV in the photoluminescence spectrum measured with the excitation of 254 nm. The measurements were taken during scanning with an electron beam over

Figure 6.4: The cathodoluminescence spectra of a structure 1 (dashed line) and 2 (solid line) of the PS sample

the area magnified by 800. Our CL results are similar to those reported by other groups [42], [72]. Suzuki et al. [72] have reported that the CL spectrum consists of two bands at 2.7 eV and 1.9 eV. They concluded that the two bands are due to different defects in amorphous SiO_x .

6.2.2 Fabrication of optical patterns

Figure 6.5 shows the cathodoluminescence profiles (a, b, c) and surface topography (secondary electron signal) (d) of the porous sample. The intensity of the CL decreases after repeated scanning at room temperature of a range of measurements. We have used this effect to make optical structures on the sample. The measurements were carried out in the same area of the sample. We have positioned the electron beam with energy of 30 keV at

Figure 6.5: The cathodoluminescence (a, b, c) and surface topography (d) of the porous sample. The written dark pattern is pointed by the arrows.

several points on the surface of sample A for 10 minutes at each point. The procedure resulted in the appearance of a dark spot pattern which is invisible in the SE image. Fig. 6.5 a shows the first dark point, Figs. 6.5 b and c show 3 and then 4 dark points, respectively, which form finally the letter "L" on the luminescence image. Comparing the CL images with the secondary electron images leads us to the conclusion that the topography of the surface of sample A has not changed during the electron beam treatment (Fig. 6.5 d). In this way, we have fabricated well-defined patterns in the porous layers of sample B. Fig. 6.6 shows the cathodoluminescence image of the written pattern "TU CHEMNITZ". The fabricated structure is about $4000\text{ }\mu\text{m}$ in total length. It is interesting to note that this pattern can be also seen under photoexcitation with UV light of 366 nm at air. The sample B shows bright red luminescence observable to the naked eye, at the same locations where the cathodoluminescence has been observed. Fig. 6.7 shows the optical microscope image of the written structure. We can clearly see

Figure 6.6: Cathodoluminescence image of a fabricated pattern : TU Chemnitz

Figure 6.7: The light microscopic image of the pattern. The bright regions shows the red luminescence.

Figure 6.8: SEM image of the region irradiated with an electron beam.

the fabricated pattern "TU CHEMNITZ" on sample B. The reduced CL and PL brightness is probably due to an electronic "damage" of the luminescent structure. The electronic effects appear to involve either changes in surface or interface states, or in the charges on the surface or on point defects in the crystallites. The dark contrast in the luminescence pictures can be described by changes in the density of non-radiative centers [241] as point defects or by a destruction of luminescent centers [78], which might be possible through the damage or modification of the delicate structure of porous silicon by high energy (30 keV) electron beam of SEM [242].

To understand the nature of the modification, that has occurred, we have performed structural and spectroscopic measurements of our written patterns. We have investigated the surface topography by SEM (Fig. 6.8). We have found a dark patch in the irradiated region. This could indicate that we have damaged or modified the delicate porous structure or the surface of porous silicon. The formation of a contamination layer could be ruled out [240], because of the short time of electron beam treatment. Mitsui et al. [78] have observed a similar effect. They have found that the electron beam irradiation generates the structural defects. For sample A, however, we have not observed any modifications of the surface structure of the irradiated region in

the SE image [243]. Here the measurements have been taken of freshly prepared PS sample. As reported in the literature [228], the skeleton surface of freshly etched PS is covered with a Si hydride layer, while that of the aged PS layers is oxidized [28]. This could indicate that different effects occur under beam irradiation for the aged and freshly prepared samples. Measuring CL with high spatial resolution requires a fine focused electron beam, hence it is possible that the measuring beam could be responsible for the same modifications in CL behaviour as mentioned in the case of optical patterning. To study this influence we have measured the CL-spectra from 1 μm diameter spot size. We have observed a marked decrease of the cathodoluminescence intensity at 2 eV and a slight decrease at 2.67 eV for the structure 2. For the structure 1, however, the intensity of the peak at 2.7 eV has changed weakly. This could indicate that we have modified or destroyed luminescence centers responsible for the emission band of ~ 2 eV. It is also interesting to note that other groups [238], [79] have observed a significant decrease or the vanishing of CL after a removing of the surface layer of porous sample. Furthermore, Mitsui et al. [78] have found the CL band at 2.95 eV at accelerating voltages higher than 160 kV at 20 K. They have proposed that the luminescence of the band at 2.95 eV arises from the interface region between the porous layer and the Si base. It could be inferred that the reduced CL and PL at ~ 2 eV is probably due to a "damage" of the luminescence centers which are in the surface (oxide) layer of porous silicon. This in turn could be a damage or a modification of the surface layer or chemical changes in this film. In contrast, the emission band at ~ 2.7 eV is unchanged, which implies that, it is a different source of luminescence. This means, based on [78] and on our results, we could say from the regions lying deeper inside the porous silicon. These facts suggest once again that there are different origins for the two emission bands.

6.3 Summary

We have fabricated a well-defined optical pattern using an electron beam as a lithographic tool. We have investigated the structure and luminescence properties of these patches by SEM, photo- and cathodoluminescence methods. We have found that the CL spectra of the porous silicon sample at 77K consists of two bands at 2 eV and at ≈ 2.7 eV. The intensity of 2 eV band peak decreases after a treatment of porous Si sample with electron beam. The band at 2.7 eV shows no significant changes after electron beam treatment. Our results indicate that luminescence modification under electron irradiation is possibly due to damage or a modification of luminescent structure on the surface layer of the PS sample [243], [244].

Chapter 7

Fabrication of microstructures of porous silicon

Conventional lithography is most certainly useful for making complicated arrays of devices and even for creating nanometer-scale devices to test quantum effects. However, it is a technique of limited flexibility.

Recently, much attention has been paid to the use of the scanning probe microscopy (SPM) as a lithographic tool, using its ability to fabricate structures from nanometer to atomic scale. It can be used to induce local modifications directly, without recourse to masks or conventional lithography. The SPM lithography has already been applied to the nano-processing of silicon, a main material used in microelectronics [245]. Particularly, scanning tunneling microscopy (STM) is a very useful tool to write nano- and microstructures onto and into the surface [246].

It is believed, however, that in the next century microelectronics will be replaced by optoelectronics, a combination of optics and electronics. Thus, the fabrication of light-emitting patterns on a micrometer scale is an important research topic.

In this chapter, we report about a fabrication of small luminescent patches

Figure 7.1: Schematic description of a fabrication of PS microstructure of using modifying STM-like device.

(diameter of a few μm) of nanoporous Si due to local anodization using a modified STM. The structure and luminescence properties of these patches have been investigated by SEM and cathodoluminescence.

7.1 Experimental Data

7.1.1 Development of ECSTM

We have developed a STM-like device (ECSTM) operated by a partially isolated probe tip for the fabrication of microstructures at the sample surface making use of an electrochemical process. Fig. 7.2 shows the head of ECSTM without control electronics. The electrochemical process was carried out in an anodization cell (Teflon), presented in Fig. 7.2 (lower part). It consists of the sample holder and the container for the HF solution. A Si-wafer and a Pt tip are used as the anode and cathode, respectively. To ensure a good electrical contact, a Pt coating was evaporated on the backside of the wafer

Figure 7.2: The STM-like device (ECSTM) set-up based on Hansma's STM (upper part) and an anodization cell (lower part)

before etching. The anodization cell could be moved in X and Y direction by the micrometer screws (Fig. 7.2 (lower part)). The distance between the tip and the Si-wafer was controlled by a stepper-motor (coarse movement) and a piezo-tube actor (PZT) with a feedback loop response (fine regulation). The PZT used here was calibrated according to the method described in [252] and has a range of about $5\text{ }\mu\text{m}/100\text{V}$ in X and Y and about $160\text{ nm}/100\text{ V}$ in Z. The tip was fixed by a small set screw in a tip holder (Teflon), which is attached to the piezo-tube. Such design allows to exchange the tip in seconds. The head is connected with the control electronics via multifunction converter (Meilhaus Electronic ME 3, 2x12 bit/2x8 bit D/A- and 12 bit A/D converter). The system is operated under computer control (for detailed descriptions see [253]).

The fabrication procedure of PS microstructure

The fabrication procedure of microstructures of porous silicon is shown in Fig. 7.3. The completely isolated tip (Fig. 7.3 a) is stepped toward the sample automatically using a stepper motor. The tip approach is stopped as soon as a tip has touched the surface, i.e. the wax layer faked off from the tip apex (Fig. 7.3 b). HF solution provides an electrical contact between tip and sample. By applying a bias voltage to the junction tip-sample (the sample is positively polarized), the surface is anodized locally at the region beneath the tip apex. This means that a Faraday current, rather than tunnelling current flows through the junction during the anodization. After moving the tip about 300 nanometers away from the sample we can start the fabrication process with required etching parameters and the distance between tip and sample (Fig. 7.3 c). Both, structural and optical properties of an etch-point are determined by the anodization parameters like current density, HF concentration, anodization time, etc, similar to porous samples prepared on a large scale (see chapter 2). The distance between tip and sample has an

Figure 7.3: Fabrication procedure of PS microstructure

Figure 7.4: SEM image of an etched Pt tip

impact on the size of the etch-point. When the fabrication process of a microstructure is finished, the anodization cell can be moved in X or Y by the micrometer screws (Fig. 7.2) and the etching process with or without changing parameters in case of need starts once again. In this way, we can create a luminescent microstructure pattern with defined optical properties.

Tip preparation

Tips for the STM can be prepared using various fabrication techniques [255], the most common are electrochemical etching and mechanical shearing. There are two preferred tip materials for STM works. These are made from either tungsten (W) or platinum (Pt) alloy wire. We have used Pt tips. Platinum, although a softer metal, is preferable to W because it is inert in the HF solution during the anodization process. The tip from Pt-wire (0.25 mm diameter) has been fabricated by electrochemical etching in a $NaCl - HNO_3$ solution, as described elsewhere [253]. The SEM image (Fig. 7.4) shows that the tip quality is reasonable. The tip is comprised of a rigid structure with a long slender region (about 500 μm long) just prior to the tip end. Its radius is approximately 50 nm (detailed description of the tip-fabrication procedure

Figure 7.5: SEM image of a wax-coated Pt tip

has been given in [253])

To protect the chemical reaction, i.e. an anodization process of sample during the tip approach, the tip must be isolated. The most difficult task was to find a proper material, because it should be not only inert within the HF solution during the fabrication procedure but easy to handle as well. To our knowledge, there are no reports about a material with such properties existing in the literature. We have tested some materials usually used as an isolation in a conventional lithography (electrodeposition lacks [256], etc.), but they were dissolved in the HF solution after the current had been supplied between tip and sample. We have found, that wax meets exactly our expectations. It is not only inert and easy to prepare but cheap as well. The Pt tip was dipped into liquid wax heated to about 60°C with the sharp end down and then even withdrawn. The procedure should be done with the tip held vertically to avoid the bending of its very fine end due to the surface tension [254]. After withdrawing, the wax on a Pt wire solidified within a few seconds. The thickness of the wax layers depends not only on the temperature of a liquid wax but on the velocity of withdrawing as well. A higher temperature and a slower velocity result in thicker wax layers. In our case, a wax layer needs

to be so thin as possible in order to reach the electrical contact just after crashing Fig. 7.5 shows a SEM image of such a completely isolated tip. The wax layer is about a few μm thick.

7.1.2 Description and characterization of samples

We have concentrated our study on the fabrication of PS microstructure and on their properties in dependence on preparation parameters. We have varied not only the current, voltage, electrolyte concentration, and etching time but the distance between the sample and tip as well. We have attached importance to the reproducibility of fabricated structures. For this purpose, we have created some patterns like the letter "L" or a simple row. Here we present a few of our results.

For the fabrication we have used p-type (boron doped) Si (100) wafers with $10\ \Omega\cdot\text{cm}$ resistivity. The etching parameters of prepared samples are given in Table 7.1

Sample	Solution $\text{HF}(40\%):\text{C}_2\text{H}_5\text{OH}$: NaNO_2	Current [mA]	Voltage [V]	Anodization time [s]	Distance tip-sample [nm]
A	1:1:0	0.1	1	30	~ 50
B	50:50:1	0.3	2	30	~ 50
C	1:1:0	0.4	5	120	~ 50

Table 7.1: Anodization parameters of samples A, B and C

The PS microstructures were investigated by SEM and cathodoluminescence (CL) (for detailed description see chapter 3). For all data presented in this

chapter the SEM was operated with 30 keV beam energy and a current density of 3 A cm^{-2} at room temperature.

7.2 Fabrication of microstructures by ECSTM

7.2.1 Structure Analysis

Fig. 7.6 shows the SEM image of fabricated microstructures (sample A). We have etched one patch and then we have moved the tip to the next place to start to etch another one. Proceeding this way, we have created five structures of porous silicon (Fig. 7.6 a). The diameter of each structure is about $20 \mu\text{m}$ and the distance between each other $\approx 30 \mu\text{m}$. Though we have not changed the anodization parameters during process we can observe some differences between them, particularly in their shape and size. In our opinion, these differences occurred due to electrical field fluctuation between tip and sample. One of the reasons could be wax remains which left on the tip apex after crashing. The fluctuations of electrolyte concentration in such a small range as the distance between sample and tip could also influence the fabrication process. In addition, the estimation of the current density enhances our assumption. If we take into account the diameter of the microstructure ($20 \mu\text{m}$) and the current (0.1 mA) we get approximately a value of a current density of order of magnitude of 10 A cm^{-2} . In this range one could expect rather an electropolishing process than a pore formation. However, as seen from Fig. 7.6 c, we can observe a quite homogeneous porous structure of an etch-patch shown on the Fig. 7.6 b. The pores and surface features are 40 to 60 nm in a diameter.

Fig. 7.7 shows the smallest microstructure of PS (sample B) fabricated by ECSTM. The diameter of this patch is about $2 \mu\text{m}$. We can observe clearly the porous structures with pores of about 100 nm.

Figure 7.6: SEM images of PS microstructures (sample A) low magnification (a), a single etch-patch (b) and (c) porous structure within a single etch-patch from (b)

Figure 7.7: SEM image of an etch-patch of 2 μm (sample B)

We have also fabricated microstructures by varying the current density. It is interesting to note, that we have not found any trace of appearance of etching process for the current between 11 and 26 μA , and at 0.8 mA, at constant other parameters. This could indicate, that higher current leads to electropolishing, whereas at the lower current the etching process occurs slower. This suggests, that the correlation between pore formation and a anodization current is strong and the value of the anodization current is limited. We have, however, not observed any significant dependencies of the radii of the etch-patches on the anodization current and the etching time. The radii of etch-patches depend mainly on two parameters: on the distance tip-sample and on the diameter of tip apex (after crashing). For a small patch diameter, one needs not only a small apex tip diameter but a small distance tip-sample as well. Our present construction of ECSTM is, however, not in position to control exactly the distance (for details see [253]) i.e. the approach and crash processes. The reference position of a tip is its position after the crash. If the tip penetrates a little bit into the sample during the crash, the distance differs from the wanted value. Thus, the crash process as well as hysteresis effects of piezoactors and a mechanical shift of the sample in X and

Figure 7.8: SEM image of an insulated Pt tip after etching

Y direction by the micrometer screws influence negatively the reproducibility of such small PS structures. In addition, as mentioned above, the geometry of the tip apex is an important parameter of the size of etch-patches. Because we can not exactly control the crash process and the thickness of the wax layer at the tip, thus, we are not able to predict the patch geometry exactly. Fig. 7.8 shows SEM image of an isolated Pt tip after etching. The Pt tip is inside a wax hollow ($\approx 100 \mu\text{m}$). One of the solutions of these problems is an exact control the distance tip-sample by a feedback loop. For this purpose one needs the application of ECSTM potentiostat or the Shear-Force technology. In the latter, the vibrating tip approach leads to an oscillation damping, which is detected by a laser. This method, however, is rather complicated and expensive.

7.2.2 Cathodoluminescence

In order to study the luminescence properties of fabricated microstructures (sample C), we have performed CL measurements. Unfortunately, we have been not able to detect a photoluminescence of the single structure due to its

Figure 7.9: SEM (a) and cathodoluminescence (b) images of an etch-patch

weak intensity resulting of its small size. The cathodoluminescence as well the porous structure of sample C are spatially inhomogenous (Fig. 7.9). The measurements were carried out in the same area of the sample. SEM image (Fig. 7.9 a) displays that the PS microstructure ($\sim 500 \mu\text{m}$ in a diameter) exhibits a relatively high surface roughness with large surface features in the range of $10 \mu\text{m}$. The surface photon map illustrates that these area, i.e. this microstructure, emits light in the wavelength range of $350\text{--}\sim 700 \text{ nm}$. We have also observed the photoluminescence of this etch-patch at UV excitation by optical microscope. It shows very intensive orange-red luminescence in the middle of the structure and green-orange on its edge.

7.3 Summary

Summarizing, we have shown that micrometer luminescent structures of porous silicon can be fabricated by a simple electrochemical STM-like device.

The cathodoluminescence of obtained patches has been detected. We have found for all our samples a strong correlation between anodization current and pore formation. The resulting microstructures have a porous structure, as commonly observed for large PS samples. Their radii depend strongly on the diameter of the tip and on the distance between tip and sample. These parameters are determined by the accuracy and quality of the ECSTM-like device. Our present construction of ECSTM is, however, not in position to exactly control them. The solution of that one can find in an exact control of the distance tip-sample by a feedback loop. For this purpose one needs the application of the ECSTM potentiostat or the Shear-Force technology. Based on our results we believe the further development of this device is worthwhile. The controlled fabrication of PS microstructures could let us not only produce various luminescent patterns in the Si-wafer but observe directly the PS structure formation as well. This may bring significant progress in integration of porous silicon into micro- and nanotechnology.

Zusammenfassung

Der Grund für die Untersuchung von porösem Silizium sind dessen Lumineszenzeigenschaften. Man kann eine Veränderung der Lumineszenzeigenschaften entweder während der Herstellung oder durch eine Nachbehandlung erzielen. In der vorliegenden Arbeit wurden reine, dotierte und strukturierte poröse Siliziumschichten untersucht. Für die optoelektronische Anwendung ist es wichtig, daß man die Lumineszenzeigenschaften des Materials kennt und sie dann kontrolliert verändern kann.

Zuerst wurden poröse Schichten sowohl auf Si-Substraten als auch abgelöst als freistehende Strukturen in Abhängigkeit von den Herstellungsparametern untersucht, wobei grundsätzlich zur Literatur ähnliche optische und strukturelle Eigenschaften gefunden wurden. Optische und Sekundärelektronenaufnahmen von freistehenden porösen Siliziumfilmen lassen die vorhergesagte Schichtstruktur erkennen. Der Ursprung dieses Effekts könnte in Inhomogenitäten im Ausgangsmaterial oder in mechanischen Spannungen, die vom Ätzprozeß herrühren, liegen. Während eine Veränderung der Konzentration der HF-Säure nur zur ebenfalls bereits beschriebenen Vertiefung der geätzten Strukturen führte, konnte bei Erhöhung der Stromdichte eine Entwicklung der Bandenstruktur im Photolumineszenzspektrum von einer zu zwei Banden beobachtet werden. Im Gegensatz zur allgemeinen Deutung gehen wir nicht von einer Verschiebung der Bande aus, sondern von dem grundsätzlichen Vorhandensein zweier Banden (1.88 eV und 2.05 eV), die

je nach Wahl der Versuchsparameter selektiv verstärkt oder abgeschwächt werden. Dies läßt sich durch die Existenz von mindestens zwei qualitativ unterschiedlichen Typen von Lumineszenzzentren erklären. Wir vermuten, daß der erste Typ von Lumineszenzzentren der Oberfläche (Oxidschicht) zuzuordnen ist, während der zweite Typ mit tieferliegenden Störstellen (Oxid bzw. Grenzfläche Oxid-Silizium) verbunden ist. Bestätigt wird diese Annahme auch dadurch, daß sich die einzelnen Lumineszenzbanden selektiv anregen lassen, sich ihre Peaklage jedoch nicht ändert. Um das Verhalten der Bandenstruktur unserer PL-Spektren zu erklären, haben wir diese mit Hilfe einer Gaußauswertung (Überlagerung von 2,3 bzw. 4 Gaußkurven) analysiert. Dabei haben wir gefunden, daß unsere Spektren generell gut durch eine Summe von zwei Gaußkurven bei 1.88 eV und 2.05 eV angepaßt werden können.

Die Skalierung der Gaußkurve, die der Darstellung des Peaks bei 2.05 eV dient, nimmt mit zunehmender Ätzstromstärke relativ zu der bei 1.88 eV zu. Ein Aufdampfen von Platin, das in der Elektronik neben Gold häufig als Kontaktschicht verwendet wird, führt zusätzlich zu einer Änderung im Verhältnis beider Lumineszenzbanden d.h. erst zur deutlichen Herausbildung der Doppelpeakstruktur in der Lumineszenz. Dies bestärkt das Modell, daß die Struktur im PL-Spektrum durch zwei oder mehrere unterschiedliche Typen von Lumineszenzzentren hervorgerufen wird. Diese Ergebnisse unterstützen insbesondere das Modell von Qin und Jia [137], daß die strahlungsbehaftete Rekombination eines in Silizium-Nanostrukturen erzeugten Elektronen-Loch Paares durch Lumineszenzzentren stattfindet.

Organische Farbstoffe sind in der Lasertechnik weit verbreitet, um durchstimmbare Laserquellen zu erhalten. Durch die Dotierung mit geeigneten Farbstoffen müßte es so möglich sein, die optischen Eigenschaften des PS nachträglich zu ändern. In unseren Experimenten wurden zur Dotierung die Farbstoffe Coumarin 153, Stilben 1, Kiton Red und Rhodamin 110 verwen-

det. Der Farbstoff ruft im wesentlichen ein Quenching aufgrund der Absorption des Farbstoffes und eine Verschiebung der Lumineszenz von PS hervor. Diese Verschiebung deutet auf eine mögliche Wechselwirkung der Farbstoffmoleküle mit PS hin. Um diesen Effekt besser zu verstehen, wurden neben PL- und PLE-Messungen auch TRF-Untersuchungen an mit Cou153 dotierten PS-Schichten gemacht. Die PL-Spektren zeigen, daß die Lumineszenz von reinem PS aus zwei Banden besteht und durch Dotierung das Intensitätsverhältnis beider Banden verändert werden kann. Man erhält eine Absenkung der Intensität des Peaks bei 1.87 eV im Vergleich zur Intensität bei 2.0 eV (bei einer Anregungswellenlänge von 254 nm). Das läßt die Schlußfolgerung zu, daß Coumarin 153 vorrangig mit einem Typ von Lumineszenzzentren wechselwirkt. Da sich das Coumarin an der Schichtoberfläche befindet, sollte es sich dabei um Lumineszenzzentren an der Oberfläche handeln. Die Ergebnisse der zeitaufgelösten Spektroskopie weisen ebenfalls auf eine Wechselwirkung zwischen PS und Coumarine 153 oder Reabsorption in der Coumarinschicht hin.

Im Rahmen dieser Arbeit wurde ein Versuchsaufbau zur Messung der Kathodolumineszenz entwickelt. Mit Hilfe dieses Aufbaus haben wir poröse Siliziumschichten untersucht. Die Kathodolumineszenz bei Raumtemperatur ist aufgrund von Oberflächeninhomogenitäten ebenfalls inhomogen und sinkt nach längerer Bestrahlung mit dem Elektronenstrahl ab. Den letzteren Effekt haben wir benutzt, um optische Muster im Mikrometerbereich im PS zu erzeugen. Diese Muster sind sowohl im Kathodolumineszenzbild als auch in der Photolumineszenz unter Anregung mit UV-Strahlung an Luft sichtbar. Die kontrastbildende reduzierte Photo- und Kathodolumineszenzintensität ist wahrscheinlich auf eine Zerstörung oder Veränderung der für die Lumineszenz verantwortlichen Struktur zurückzuführen. Um die Natur der damit verbundenen Modifikationen im PS zu verstehen, haben wir topographische und spektroskopische CL-Messungen der geschriebenen Muster durchgeführt.

Im Sekundärelektronenbild ist ein dunkler Punkt in der bestrahlten Region zu beobachten, der unserer Vermutung nach von einer Zerstörung der PS-Struktur herrührt. Die Entstehung einer Kontaminationsschicht kann aufgrund der kurzen Bestrahlungszeiten mit dem Elektronenstrahl ausgeschlossen werden. Spektrale CL-Messungen zeigen bei unbehandelten PS-Schichten zwei Banden bei 2.7 eV und 2.0 eV. In den erzeugten optischen Mustern ist jedoch nur eine Bande bei 2.7 eV beobachtbar. Basierend auf unseren oben erwähnten Ergebnissen (dotierte und reine Proben) kann vermutet werden, daß die Bande bei 2.0 eV von Störstellen in der Oberflächen(oxid)schicht hervorgerufen wird und diese im Fall der Bestrahlung mit einem Elektronenstrahl modifiziert oder zerstört wird. Im Gegensatz dazu stammt die Kathodolumineszenz bei 2.7 eV von tieferliegenden Störstellen im SiO_x , was mit in der Literatur zu findenden Ergebnissen übereinstimmt.

Für die Anwendung in der Optoelektronik ist es nicht nur wichtig, die Lumineszenzeigenschaften lokal zu modifizieren, sondern auch lumineszierende Strukturen im Mikrometerbereich anfertigen zu können. Während dieser Arbeit wurde ein STM-ähnliches Gerät zur Erzeugung von lumineszierenden porösen Siliziummikrostrukturen durch einen elektrochemischen Prozeß entwickelt. Die damit gewonnenen lumineszierenden Strukturen wurden mit einem SEM sowie durch Kathodolumineszenzmessungen untersucht. Die poröse Struktur im Innern des Ätzpunktes zeigt starke Ähnlichkeit zu den herkömmlich gefertigten makroskopischen PS-Proben. Es kann eine enge Korrelation zwischen Ätzstrom und Strukturbildungsprozeß festgestellt werden. Im Gegensatz dazu konnte kein Einfluß des Ätzstromes auf den Durchmesser des Ätzpunktes gefunden werden. Dieser hängt hauptsächlich von der Geometrie der Spitze und dem Abstand Probe-Spitze ab. Die Größe der hergestellten porösen Strukturen liegt im Bereich von $1.5\ \mu m$ (die kleinste hier erzeugte PS-Struktur) bis $500\ \mu m$.

Bibliography

- [1] L. T. Canham: Appl. Phys. Lett. **57**, 1046 (1990)
- [2] R. W. Fathauer, T. George, A. Ksendzow, R. P. Vaquez: Appl. Phys. Lett. **60**, 995 (1992)
- [3] R. E. Hummel, S.-S. Chang: Appl. Phys. Lett. **61**, 1965 (1992)
- [4] M. Rückschloss, O. Ambacher, S. Veprek: J. Lumin. **57**, 1 (1993)
- [5] R. L. Smith, S. D. Collins: J. Appl. Phys. **71**, R1 (1992)
- [6] J. B. Flynn: J. Electroanal. Chem. **280**, 297 (1958)
- [7] D. R. Turner: The Electrochemistry of Semiconductors, (Academic, London), 179 (1962)
- [8] A. K. Vijh: Encyclopedia of Electrochemistry of the Elements, (Dekker, New York) **5**, 287 (1986)
- [9] H. Foll: Appl. Phys. A **53**, 8 (1991)
- [10] X. G. Zhang, S. D. Collins, R. L. Smith, J. Electrochem. Soc. **136**, 1561 (1989)
- [11] V. Lehmann: Adv. Mater. **4**, 762 (1992)
- [12] M. I. J. Beale, J. D. Benjamin, M. J. Uren, N. G. Chew, A. G. Cullis: J. Cryst. Growth **73**, 622 (1985)

- [13] V. Lehmann, H. Foll: J. Electrochem. Soc. **135**, 2831 (1988)
- [14] M. Schoisswohl, J. L. Cantin, H. J. von Bardeleben, G. Amato: Appl. Phys. Lett. **66**, 3660 (1995)
- [15] M. Mizuta: Acta Phys. Polon. **84**, 609 (1993)
- [16] D. Rüter, T. Kunze, W. Bauhofer: Appl. Phys. Lett. **64**, 3006 (1994)
- [17] S. Veprek, V. Marecek: Solid State Electron. **11**, 683 (1993)
- [18] M. I. J. Beale, I. D. Benjamin, M. J. Uren, N. G. Chew, A. G. Cullis, Appl. Phys. Lett. **46**, 86 (1985)
- [19] L. Niemeyer, L. Pietronero, H. J. Wiesmann, Phys. Rev. Lett. **52**, 1033 (1984)
- [20] R. L. Smith, S.-F. Chuang, S. D. Collins: J. Electron. Mater. **17**, 533 (1988)
- [21] V. Lehmann, U. Gösele: Appl. Phys. Lett. **58**, 856 (1991)
- [22] A. Halimaoui, C. Oules, G. Bomchil, A. Bsiesy, F. Gaspard, R. Herino, M. Ligeon, F. Müller: Appl. Phys. Lett. **59**, 304 (1991)
- [23] A. Bsiesy, J. C. Vial, F. Gaspard, R. Herino, M. Ligeon, F. Müller, R. Romestain, A. Wasiela, A. Halimaoui, G. Bomchil: Surf. Sci. **254**, 195 (1991).
- [24] S. Frohnhoff, Diplomarbeit, RTWH Aachen, 1993, S. Frohnhoff, in Berichte des Forschungszentrum Jülich, Jül-2765, ISSN 0944-2952.
- [25] S.-F. Chuang, S. D. Collins, R. L. Smith: Appl. Phys. Lett. **55**, 675 (1989)
- [26] A. Nishida, K. Nakagawa, H. Kakibayashi, T. Shimada: Jpn. J. Appl. Phys. **31**, L1219 (1992)

- [27] L. T. Canham, M. R. Houlton, W. Y. Leong, C. Pickering, J. M. Keen: J. Appl. Phys **70**, 422 (1992)
- [28] Y. H. Xie, W. L. Wilson, F. M. Ross, J. A. Mucha, E. A. Fitzgerald, J. M. Macaulay: J. Appl. Phys. **71**, 2403 (1992)
- [29] H. Münder, C. Andrzejak, M. G. Berger, T. Eickhoff, H. Lüth, W. Theiss, U. Rossow, W. Richter, R. Herino, M. Ligeon: Appl. Surf. Sci. **56**, 6 (1992)
- [30] Y. Sasaki, M. Kitahara: J. Appl. Phys. **76**, 4344 (1994)
- [31] H. Münder, M. G. Berger, S. Frohnhoff, M. Thönissen, H. Lüth: J. Lumin., 1042 (1993)
- [32] K. Barla, G. Bomchil, R. Herino, J. C. Pfister: J. Cryst. Growth **68**, 721 (1984)
- [33] I. M. Young, M. I. J. Beale, J. E. Benjamin: Appl. Phys. Lett. **46**, 1133 (1985)
- [34] R. Herino, G. Bomchil, K. Barla, C. Bertrand: J. Electrochem. Soc. **134**, 1994 (1987)
- [35] L. Wang, M. T. Wilson, M. S. Goorsky, N. M. Haegel: Mater. Res. Soc. Symp. Proc. **256**, 73 (1992)
- [36] Y. Kanemitsu, K. Suzuki, H. Uto, Y. Masumoto, T. Matsumoto, S. Kyushin, K. Higuchi, H. Matsumoto: Appl. Phys. Lett. **61**, 2446 (1992)
- [37] A. A. Andrianov, D. I. Kovalev, U. B. Shuman, I. D. Yaroshetskii: JEPT Lett. **56**, 943 (1992)
- [38] P. D. Calcott, K. J. Nash, L. T. Canham, M. J. Kane, D. Brumhead: J. Phys. Condens. Matter **5**, L91 (1993)

- [39] M. K. Lee, K. R. Peng: Appl. Phys. Lett. **62**, 3159 (1993)
- [40] D. I. Kovalev, I. D. Yaroshetskii, T. Muschlik, V. Petrova-Koch, F. Koch: Appl. Phys. Lett. **64**, 214 (1994)
- [41] L. Tsybeskov, Ju. V. Vandyshev, P. M. Fuuchet: Phys. Rev. B **49**, 7821 (1994)
- [42] A. G. Cullis, L. T. Canham, G. M. Williams, P. W. Smith, O. D. Dosser: J. Appl. Phys. **75**, 493 (1994)
- [43] G. Mauckner, J. Hamann, W. Rebitzer, T. Baier, K. Thonke, R. Sauer: Mater. Res. Soc. Symp. **358**, 489 (1995)
- [44] S. M. Prokes: Appl. Phys. Lett. **62**, 3244 (1993)
- [45] S. Shih, C. Tsai, K.-H. Li, K. H. Jung, J. C. Campbell, D. L. Kwong: Appl. Phys. Lett. **60**, 633 (1992)
- [46] V. Petrova-Koch, T. Muschlik, A. Kox, B. K. Meyer, F. Koch: Appl. Phys. Lett. **61**, 943 (1992)
- [47] T. Maruyama, S. Ohtani: Appl. Phys. Lett. **65**, 1346 (1994)
- [48] S. Gardelis, J. S. Rimmer, P. Dawson, B. Hamilton, R. A. Kubiak, T. E. Whall, E. H. C. Parker: Appl. Phys. Lett. **59**, 2118 (1991)
- [49] T. von Buuren, Y. Gao, T. Tiedje, J. R. Dahn, B. M. Way: Appl. Phys. Lett. **60**, 3013 (1992)
- [50] X. Y. Hou, G. Shi, W. Wang, F. L. Zhang, P. H. Hao, D. M. Huang, X. F. Jin, X. Wang: Mater. Res. Soc. Symp. Proc. **283**, 89 (1993)
- [51] X. Zhao, O. Schoenfeld, Y. Aoyagi, T. Sugano: Appl. Phys. Lett. **65**, 1290 (1994)

- [52] T. Matsumoto, M. Daimon, T. Futagi, H. Mimura: Jpn. J. Appl. Phys. **31**, L619 (1992)
- [53] N. Ookubo, H. Ono, Y. Ochiai, Y. Mochizuki, S. Matsui: Appl. Phys. Lett. **61**, 940 (1992)
- [54] J. C. Vial, A. Bsiesy, F. Gaspard, R. Herino, M. Ligeon, F. Muller, R. Romestain, R. M. Macfarlane: Phys. Rev. B **45**, 14171 (1992)
- [55] R. Piazza, T. Bellini, V. Degiorgio: Phys. Rev. B **38**, 7223 (1988)
- [56] Y. Mochizuki, M. Mizuta, Y. Ochiai, S. Matsui, N. Ohkubo: Phys. Rev. B. **46**, 12353 (1992)
- [57] Y. Mochizuki, M. Mizuta: Mat. Science Forum **117-118**, 507 (1993)
- [58] C. Tsai, K. H. Li, J. Sarathy, S. Shih, J. C. Campbell: Appl. Phys. Lett. **59**, 2814 (1991)
- [59] Z. Y. Xu, M. Gal, M. Gross: Appl. Phys. Lett. **60**, 1375 (1992)
- [60] M. A. Tischler, R. T. Collins, J. H. Stathis, J. C. Tsang: Appl. Phys. Lett **60**, 639 (1992)
- [61] R. T. Collins, M. A. Tischler, J. H. Stathis: Appl. Phys. Lett. **61**, 649 (1992)
- [62] L. E. Friedersdorf, P. C. Searson, S. M. Prokes, O. J. Glembocki, J. M. Macaulay: Appl. Phys. Lett. **60**, 1532 (1992)
- [63] N. Koshida, H. Koyama: Appl. Phys. Lett. **60**, 347 (1992)
- [64] A. Richter, P. Steiner, F. Kozlowski, W. Lang: IEEE Electron Device Lett. **EDL-12**, 691 (1991)
- [65] F. Namavar, H. P. Maruska, N. M. Kalkhoran: Appl. Phys. Lett. **60**, 2514 (1992)

- [66] H. P. Maruska, F. Namavar, N. M. Kalkhoran: Appl. Phys. Lett **61**, 1338 (1992)
- [67] T. Futagi, T. Matsumoto, M. Katsuno, Y. Ohta: Appl. Phys. Lett **63**, 1209 (1993)
- [68] L. T. Canham, W. Y. Leong, M. I. J. Beale, T. I. Cox, L. Taylor: Appl. Phys. Lett. **61**, 2563 (1992)
- [69] M. Enachescu, E. Hartmann, A. Kux, F. Koch: Proceedings of the 21st ICPS (World Scientific, Signapore, 1993), pp. 1439
- [70] Z. Chen, T.-Y. Lee, G. Bosman: Appl. Phys. Lett. **64**, 3446 (1994)
- [71] Luminescence Spectroscopy, ed. M. D. Lumb (Academic Press, New York, 1978), p. 171
- [72] T. Suzuki, T. Sakai, L. Zhang, Y. Nishiyama: Appl. Phys. Lett. **66**, 215 (1995)
- [73] S. W. Mcknight, E. D. Palik: J. Non-cryst. Solids **40**, 595 (1980)
- [74] F. Pio, M. Guzzi, G. Spinolo, M. Martini: Phys. Stat. Sol. B **159**, 577 (1990)
- [75] L. N. Skuja, W. Eritzian: Phys. Status Solidi A **96**, 191 (1986)
- [76] A. R. Silin, L. N. Skuja, A. V. Shendrik: Fiz. Khim. Stekla **4**, 405 (1978)
- [77] S. Munekuni, T. Yamanaka, Y. Shimogaichi, R. Tohmon, Y. Ohki: J. Appl. Phys. **68**, 1212 (1990)
- [78] T. Mitsui, N. Yamamoto, K. Takemoto, O. Nittono: Jpn. J. Appl. Phys. **33**, L342 (1994)
- [79] S. M. Pillai, Z. Y. Xu, M. Gal, R. Glaisher, M. Philips and D. Cockayne: Jpn. J. Appl. Phys. **31**, L1702 (1992)

- [80] K. Tanimura, T. Tanaka, N. Itoh: Phys. Rev. Lett. **51**, 423 (1983)
- [81] T. Ohta, O. Arakaki, T. Ito, A. Hiraki: IEICE Trans. Electron. **E75-C**, 1025 (1992)
- [82] J. F. Harvey, H. Shen, R. A. Lux, M. Dutta, J. Pamulapati, R. Tsu: in Light Emission from Silicon, edited by S. S. Iyer, R. T. Collins, L. T. Canham (Materials Research Society, Pittsburgh, PA, 1992), pp. 175-178
- [83] C. Tsai, K.-H. Li, D. S. Kinosky, R.-Z. Qian, T.-C. Hsu, J. T. Irby, S. K. Banerjee, A. F. Tasch, J. C. Campbell, B. K. Hance, J. M. White : Appl. Phys. Lett. **60**, 1700 (1992)
- [84] M. S. Brandt, H. D. Fuchs, M. Stutzmann, J. Weber, M. Cardona: Solid State Commun. **81**, 307 (1992)
- [85] S. M. Prokes, O. J. Glembocki, V. M. Bermudez, R. Kaplan, L. E. Friedersdorf, P. C. Searson: Phys. Rev. B **45**, 13788 (1992)
- [86] D. J. Wolford, B. A. Scott, J. A. Reiner, J. A. Bradley: Physica **117B** & **118B**, 920 (1983)
- [87] V. Petrova-Koch, T. Muschlik, D. I. Kovalev, F. Koch, V. Lehmann: Mater. Res. Soc. Symp. Proc. **283**, 179 (1993)
- [88] B. Delley, E. F. Steigmeier: Phys. Rev. B **47**, 1397 (1993)
- [89] C. Delerue, G. Allan, M. Lannoo: Phys. Rev. B **48**, 11024 (1993)
- [90] L. E. Brus: J. Phys. Chem. **90**, 2555 (1986)
- [91] V. L. Colvin, A. P. Alivisatos, J. G. Tobin: Phys. Rev. Lett. **66**, 2786 (1991)

- [92] H. Morisaki, H. Hashimoto, F. W. Ping, H. Nozawa, H. Ono: J. Appl. Phys. **74**, 2977 (1993)
- [93] V. Vezin, P. Goudeau, A. Naudon, A. Halimaoui, B. Lambert, G. Bomchil: Appl. Phys. Lett. **60**, 2625 (1992)
- [94] H. Takagi, H. Ogawa, Y. Yamazaki, A. Ishizaki, T. Nakagiri: Appl. Phys. Lett. **56**, 2379 (1990)
- [95] X. L. Zheng, W. Wang, H. C. Chen: Appl. Phys. Lett. **60**, 986 (1992)
- [96] W. Zhou, H. Shen, J. F. Harvey, R. A. Lux, M. Dutta, F. Lu, C. H. Perry, R. Tsu, N. M. Kalkhoran, F. Namavar: Appl. Phys. Lett. **61**, 1435 (1992)
- [97] W. Paul, D. M. Warschauer, Solid unter Pressure (MacGraw-Hill, New York, 1963), p.222
- [98] F. Koch, V. Petrova-Koch, T. Muschlik, A. Nikolov, V. Gavrilenco: Mater. Res. Soc. Symp. Proc. **283**, 197 (1993)
- [99] J. Lin, L. Z. Zhang, Y. M. Huang, B. R. Zhang: Appl. Phys. Lett. **64**, 3282 (1994)
- [100] M. Stutzmann, M. S. Brandt, M. Rosenbauer, J. Weber, H. D. Fuchs, Phys. Rev. B **47**, 4806 (1993)
- [101] M. Stutzmann, M. S. Brandt, E. Bustarret, H. D. Fuchs, M. Rosenbauer, A. Höpner, J. Weber: J. Non-cryst. Solids **164**, 931 (1993)
- [102] P. Deak, M. Rosenbauer, M. Stutzmann, J. Weber, M. S. Brandt: Phys. Rev. Lett. **69**, 2531 (1992)
- [103] K. Takeda, K. Shiraishi: Solid State Commun. **85**, 301 (1993)

- [104] H. Ubara, T. Imura, A. Hiraki, I. Hirabayashi, K. Morigaki: J. Non-cryst. Solids **59-60**, 641 (1983)
- [105] H. Münder, M. G. Berger, S. Frohnhoff, H. Lüth, U. Rossow, H. Frotscher, W. Richter; Mat. Res. Soc. Symp. Proc. **283**, 281 (1993)
- [106] H. Kautsky, G. Herzberg: Z. anorg. u. allg. Chem. **139**, 135 (1924)
- [107] M. B. Robinson, A. C. Dillon, D. R. Haynes, S. M. George: Mater. Res. Symp. Proc. **256**, 17 (1992)
- [108] K. Takeda, K. Shiraishi: Phys. Rev. B **39** 11028 (1989)
- [109] K. Tanimura, C. Itoh, N. Itoh: J. Phys. C **21**, 1869 (1988)
- [110] R. A. Street: Semiconductors and Semimetals, Vol. 21, Academic Press, New York, part B, p.197
- [111] E. Bustarret, J. Cali, Y. Cros, M. Brunel, I. Mihalcescu, M. Ligeon : J. Non-cryst. Solids **164-166**, 937 (1993)
- [112] F. Koch: Mater. Res. Soc. Symp. Proc. **298**, 319 (1993)
- [113] K. Murayama, S. Miyazaki, M. Hirose: Jpn. J. Appl. Phys. **31**, L1358 (1992)
- [114] K. Cho, Y. Toyozawa: J. Phys. Soc. Jpn. **30**, 1555 (1971)
- [115] R. Laiho, A. Pavlov, T. Tsuboi : J. Lumin. **57**, 89 (1993)
- [116] J. H. Stathis, M. A. Kastner: Phys. Rev. B **35**, 2972 (1987)
- [117] H. Stintzig: DRP **481**, 155 (1927/1929)
- [118] M. Knoll: Z. Techn. Phys. **16**, 767 (1935)
- [119] K. Wetzig, D. Schulze: In situ Scanning Electron Microscopy in Materials Research; Berlin: Akad. Verlag 1995

- [120] D. J. O'connor, B. A. Sexton, R. St. C. Smart: Surface Analysis Methods in Material Science, Springer-Verlag, Berlin Heidelberg 1992
- [121] Handbook of Sputter Deposition Technology Principles, Technology and Applications by Kiyotaka Wasa, Shigeru Hayakawa, Noyes Publications, Park Ridge, New Jersey, USA 1992
- [122] L. Reimer: Transmission Electron Microscopy, 2nd edn., Springer Ser. Opt. Sci., Vol.36 (Springer, Berlin, Heidelberg 1989)
- [123] H.-J. Güntherodt, R. Wiesendanger: Scanning Tunneling Microscopy I, Springer-Verlag Berlin, Heidelberg 1992, 1994
- [124] M. Hietschold, C. Hamann: Raster- Tunnel-Mikroskopie; Aufbau Verlag GmbH, Berlin 1991
- [125] G. Binnig, H. Rohrer, Ch. Gerber, E. Weibel: Phys. Rev. Lett. **49**, 57 (1982)
- [126] G. Binnig, H. Rohrer: Surf. Sci. **126**, 236 (1983)
- [127] G. Binnig, H. Rohrer, Ch. Gerber, E. Weibel: Phys. Rev. Lett. **50**, 120 (1983)
- [128] A. Bryant, D. P. E. Smith, C. F. Quate: Appl. Phys. Lett. **48**, 832 (1986)
- [129] P. K. Hansma: J. Appl. Phys. **61**, R1 (1987)
- [130] E. M. Davis, Fu-Ren Fan, A. J. Bard: J. Electroanal. Chem. **238**, 9 (1987)
- [131] H. Siegenthaler, R. Christoph: In Situ Scanning Tunneling Microscopy and Related Methods, ed. by R. J. Behm, N. Garcia, H. Rohrer, NATO ASI Series E, Vol. 184 (Kluwer, Dordrecht, 1990) pp. 315-333

- [132] R. Sonnenfeld, P. K. Hansma: *Science* **232**, 211 (1986)
- [133] O. Lev, Fu-Ren Fan, A. J. Bard: *J. Electrochem. Soc.* **135**, 783 (1988)
- [134] P. Lustenberger, H. Rohrer, R. Christoph, H. Siegenthaler: *J. Electroanal. Chem.* **243**, 225 (1988)
- [135] J. Wiechers, T. Twomey, D. M. Kolb, R. J. Behm: *J. Electroanal. Chem.* **248**, 451 (1988)
- [136] R. Wiesendanger, H.-J. Güntherodt: *Scanning Tunneling Microscopy II*, Springer- Verlag Berlin Heidelberg 1992
- [137] G. G. Qin, Y. Q. Jia, *Solid State Commun.* **86**, 559 (1993)
- [138] F. Koch, V. Petrova-Koch, T. Muschik: *J. Lumin.* **57**, 271 (1993)
- [139] S. M. Prokes, O. J. Glembocki: *Phys. Rev. B* **49**, 2238 (1994)
- [140] A. J. Kontkiewicz, A. M. Kontkiewich, J. Siejka, S. Sen, G. Nowak, A. M. Hoff, P. Sakthivel, K. Ahmed, P. Mukherjee, S. Witanachchi, J. Lagowski: *Appl. Phys. Lett.* **65**, 1436 (1994)
- [141] B. Pivac, B. Ravkin, L. Pavesi: *Appl. Phys. Lett.* **65**, 3260 (1994)
- [142] J. Q. Duan, G. Q. Yao, H. Z. Song, B. R. Zhang, L. Z. Zhang, G. G. Qin: *J. Appl. Phys.* **78**, 478 (1995)
- [143] P. L. Mattern, K. Lengweiler, P. W. Levy: *Radiat. Eff.* **26**, 237 (1975)
- [144] G. H. Sigel, Jr. and M. J. Marrone: *J. Non-cryst. Solids* **45**, 235 (1981)
- [145] L. A. Balagurov, B. M. Leiferov, E. A. Petrova, A. F. Orlov, E. M. Panasenko: *J. Appl. Phys.* **79**, 7143 (1996)
- [146] H.-J. Lee, Y. H. Seo, D.-H. Oh, K. S. Nahm, Y. B. Hahn, I. C. Jeon, E.-K. Suh, Y. H. Lee, H. J. Lee: *J. Appl. Phys.* **75**, 8060 (1994)

- [147] S.-L. Zhang, K. S. Ho, Y. Hou, B. Qian, P. Diao, S. Cai, Appl. Phys. Lett. **62**, 642 (1993)
- [148] A. Bsiesy, F. Muller, M. Ligeon, F. Gaspard, R. Herino, R. Romestain, J. C. Vial: Phys. Rev. Lett. **71**, 637 (1993)
- [149] E. V. Astrova, A. A. Lebedev, A. D. Remenok Yu V. Rud, Fiz. Tekh. Poluprovodn. **28**, 493 (1994) [Semiconductors **28**, 302 (1994)]
- [150] M. Kondo, J. Non-cryst. Solids **164-166**, 941 (1993)
- [151] J. Freund, Ann. Physik **1**, 380 (1992)
- [152] W. J. Dixon, F. J. Massey, Introduction to statistical analysis, McGraw-Hill (1969)
- [153] R. A. Street, Hydrogenated Amorphous Silicon (Cambridge University, Cambridge, 1991), p.298
- [154] J. C. Knights, R. A. Street, and G. Lucovsky, J. Non-cryst. Solids **35**, 279 (1980)
- [155] H. Kaneko, P. J. French and R. F. Wolffenbuttel, J. Lumin. **57**, 101 (1993)
- [156] A. G. Cullis and L. T. Canham, Nature **353**, 335 (1991)
- [157] K. Murayama, S. Miyazaki and M. Hirose, Jpn. J. Appl. Phys. **33**, 3310 (1994)
- [158] E. Takasuka, K. Kamei: Appl. Phys. Lett. **65**, 484 (1994)
- [159] G. W. t'Hooft, Y. A. R. R. Kessener, G. L. J. A. Rikken, A. H. J. Venhuizen: Appl. Phys. Lett **61**, 2344 (1992)
- [160] M. Rosenbauer, H. Fuchs, M. Stutzmann: Appl. Phys. Lett. **63**, 565 (1993)

- [161] V. M. Asnin, N. S. Averkiev, A. B. Churilov, I. I. Markov, N. E. Mokrousov, A. Yu. Silov, V. I. Stepanov: Solid State Commun. **87**, 817 (1993)
- [162] L. Suemune, N. Noguchi, M. Yamanishi: Jpn. J. Appl. Phys. **31**, L494 (1992)
- [163] N. S. Averkiev, V. M. Asnin, I. I. Markov, A. Yu. Silov, V. I. Stepanov, A. B. Churilov, N. E. Mokrousov: JETP Letters **55**, 659 (1992)
- [164] J. Fujiwara, H. Nishitani, et al. : Jpn. J. Appl. Phys. Lett. **63**, 565 (1993)
- [165] E. V. Astrova, A. A. Lebedev, A. D. Remenyuk, Yu. V. Rud: Zh. Tekh. Fiz. **20**, 33 (1994), Tech. Phys. Lett. **20**, 622 (1994)
- [166] T. Matsumoto, T. Futagi, N. Mimura, Y. Kanemitsu: Phys. Rev. B **47**, 13 876 (1993)
- [167] B. K. Meyer, D. M. Hoffmann, W. Stadler, V. Petrova-Koch, F. Koch, P. Omling, P. Emanuelson: Appl. Phys. Lett. **63**, 2120 (1993)
- [168] L. N. Skuja, A. R. Silin: Phys. Stat. Sol. (a) **56**, K11 (1979)
- [169] C. Itoh, T. Suzuki, N. Itoh: Phys. Rev. B **41** , 3794 (1990)
- [170] Properties of Silicon, INSPEC, The Institution of Electrical Engineers, London and New York ,777 (1988)
- [171] H. Münder, M. G. Berger, St. Frohnhoff, M. Thönissen, H. Lüth, W. Theiß, L. Küpper: Optical Properties of Low Dimensional Silicon Structures, 75-80, 1993 Kluwer Academic Publishers, Netherlands.
- [172] V. Grivickas, J. Linnros, J. A. Tellefsen: E-MRS 1994 Strasbourg
- [173] S. Sawada, N. Hamada, N. Ookubo: Phys. Rev. B **49**, 5236 (1994)

- [174] T. P. Pearsall, Jen C. Adams, Jen E. Wu, Brett Z. Nosho, Chak Aw, J. C. Patton, J. Appl. Phys. **71**, 4470 (1992)
- [175] M. A. Tischler, R. T. Collins: Solid State Commun. **84**, 819 (1992)
- [176] S. Nakajima, Y. Toyozawa, R. Abe: The Physics of Elementary Excitations (Springer-Verlag, Berlin, Heidelberg, New York, 1980), Solid-State Sciences Vol. 12, Chap.7
- [177] S. Finkeberg, Dissertation
- [178] T. Miyoshi, K. S. Lee, Y. Aoyagi: J. Appl. Phys. **31**, 2470 (1992)
- [179] C. Tsang, R. A. Street: Phys. Rev. B **19**, 3027 (1979)
- [180] A. J. Read¹, R. J. Needs, K. J. Nash, L. T. Canham, P. D. J. Calcott, A. Qteish: Phys. Rev. Lett. **69**, 1232 (1992)
- [181] F. Buda, J. Kohanoff, M. Parrinello: Phys. Rev. Lett. **69**, 1272 (1992)
- [182] L. R. Tessler, F. Alvarez, O. Teschke: Appl. Phys. Lett. **62**, 2381 (1993)
- [183] Y. Sasaki, C. Horie: Proceedings of Int. Conf. on Optical Properties of Nanostructures, Sendai, 1994
- [184] M. Ueta, H. Kanzaki, K. Kobayashi, Y. Toyozawa, E. Hanamura, Excitonic Processes in Solids, p. 245. Springer-Verlag, Berlin- Heidelberg-New York-Tokyo (1986)
- [185] K. Murayama, S. Miyazaki, M. Hirose: Solid State Commun. **93**, 841 (1995)
- [186] Y. Kanemitsu, T. Ogawa, K. Shiraishi, K. Takeda: Phys. Rev. B **48**, 4883 (1993)
- [187] C. H. Perry, F. Lu, F. Namavar, N. M. Kalkhoran, R. A. Soref: Mater. Res. Soc. Symp. Proc. **256**, 153 (1992)

- [188] V. N. Abakumov, V. I. Perel, I. N. Yassievich: Nonradiative Recombination in Semiconductors (North-Holland, Amsterdam, 1991) Chap.11
- [189] D. L. Naylor, S. B. Lee, J. C. Pincenti, B. E. Bouma: Mater. Res. Soc. Symp. Proc. **256**, 111 (1992)
- [190] K. Murayama, H. Komatsu, S. Miyazaki, M. Hirose: Jpn. J. Appl. Phys. **34**, 176 (1995)
- [191] G. Dolling, R. A. Cowley: Proc. Phys. Soc. London **88**, 463 (1966)
- [192] P. Basmaji, G. Surdutovich, R. Vitlina, J. Kolenda, V. S. Bagnato: Solid State Commun. **91**, 649 (1994).
- [193] M. J. Sailor, K. L. Kavangh: Adv. Mater. **4**, 432 (1992).
- [194] T. George, M.S. Anderson, W. T. Pike, T. L. Lin, R. W. Fathauer, Appl. Phys. Lett. **60**, 2359 (1992).
- [195] V. Lehman, B. Jobst, Th. Muschnik, A. Kux, V. Petrova-Koch: Jpn. J. Appl. Phys. **32**, 2095 (1993).
- [196] V. Lehman: Thin Solid Films **255**, 1 (1995).
- [197] V. Lehman: J. Electrochem. Soc. **140**, 2837 (1993).
- [198] Y. H. Xie, M. S. Hibertsen, W. L. Wilson, S. A. Ipri, G. E. Carver, W. L. Brown, E. M. Dons, B. E. Weir, A. R. Kortan, G. P. Watson, A. J. Liddle: Phys. Rev. B **49**, 5386 (1994).
- [199] J. von Behner, L. Tsybeskov, P. M. Fauchet: Mat. Res. Soc. Symp. Proc. **358**, 333 (1995).
- [200] G. Mauckner, W. Rebitzer, K. Thonke, R. Sauer: Solid State Commun. **91**, 717 (1994).

- [201] H. Tanino, A. Kuprin, H. Deai, N. Koshida: Phys. Rev. B. **53**, 1937 (1996)
- [202] A. Bruska, E.V. Astrova, U. Falke, T. Raschke, M. Radehaus and M. Hietschold; E-MRS 1996 Spring Meeting, June 4-7, 1996, Strasbourg, France; Thin Solid Fims (accepted)
- [203] J. C. Owrutsky, J. K. Rice, S. Guha, P. Steiner, W. Lang: Appl. Phys. Lett. **67**, 1966 (1995)
- [204] D. R. Turner: J. Electrochem. Soc. **105**, 402 (1958)
- [205] M. Stutzmann, M. S. Brandt, M. Rosenbauer, H. D. Fuchs, S. Finkbeiner, J. Weber, P. Deak: J. Luminesc. **57**, 321 (1993).
- [206] H.-W. Rotter, Glimmer und Glimmererzeugnisse. Siemens Aktiengesellschaft. Berlin, München, 136 (1985).
- [207] Transistor Technology, ed. by H. E. Bridgers, J. H. Scaff, J. N. Shive, F. J. Biondi, D. van Norstard Comp., Inc., 1958.
- [208] G. K. Moroz, A. V. Zherzdev, Semiconductors 28, 550 (1994).
- [209] S. Frohnhoff, M. G. Berger: Adv. Mater. **6**, 963 (1994).
- [210] M. G. Berger, R. Arens-Fischer, S. T. Frohnhoff, C. Dieker, K. Winz, H. Münder, H. Lüth, M. Arntzen, W. Theiss, Mat. Res. Symp. Proc. **358**, 327 (1995).
- [211] M. Rosenbauer, Ph.D work, München 1995
- [212] L. T. Canham, A. G. Cullis, C. Pickering, O. D. Dosser, T. I. Cox, T. P. Lynch: Nature **368**, 133 (1994)
- [213] U. Brackmann, Lambdachrome Laser Dyes, Lambda Physik, Göttingen 1986

- [214] D. Schneider, T. Schwarz, H.- P. Buchkremer, D. Stöver: Thin Solid Films **224**, 177 (1993)
- [215] H. Morisaki and S. Nozaki, Visible Light Emission from Si Nanostructures, in: Physics, Chemistry and Application of Nanostructures, eds. V. E. Borisenko, A. B. Filonov, S. V. Gaponenko and V. S. Gurin, Belarusian State University of Informatics and Radioelectronics, Minsk, 1995, p.18
- [216] A. Bruska, M. Hietschold and C. von Borczyskowski, Various Mechanisms of Porous Silicon Photoluminescence, in preparation.
- [217] P. K. Kashrarov, E. A. Konstantivova, S. A. Petrova, V. Yu. Timoshenko, A. E. Yunovich, Excitonic Effects in Luminescence of Porous Silicon. Post-Deadline Paper. International Conference "NANOMEETING-95", Minsk, Belarus, 15-19.05.1995
- [218] M. Kasha, Molecular Excitons in Small Aggregates, Plenum Publishing Corp., New York, 1976, p.337.
- [219] Th. Förster, Fluoreszenz organischer Verbindungen, Vandenhöck und Ruprecht, Göttingen, 1951, p.312.
- [220] A. N. Starukhin, A. A. Lebedev, B. S. Razbirin and I. M. Kapitonova: Sov. Tech. Phys. Lett. **18**, 535 (1992)
- [221] F. A. d'Avitaya, F. Bassani, L. Vervoort, A. G. Nassioupoulos, S Grigoropolous, E. Gogolides, I. Mihalcescu, J. C. Vial: Silicon Nanostructures: A Way for Si Optoelectronics, eds. V. E. Borisenko, A. B. Filonov, S. V. Gaponenko and V. S. Gurin, Belarusian State University of Informatics and Radioelectronics, Minsk, 1995, p.1
- [222] E. I. Zenkevich, A. V. Chernook, A. M. Shulga, P. P. Pershukevich, G. P. Gurinovich and E. I. Sagun: Khimicheskaya Fizika **10**, 1183 (1991)

- [223] S. J. Raider, R. Flitsch and M. J. Palmer, *J. Electrochem. Soc.* **122**, 413 (1975)
- [224] *Dye Lasers, Topics in Applied Physics*, (ed. by F. P. Schafer) Springer Berlin, 1977.
- [225] S. V. Gaponenko, I. N. Germanenko, A. P. Stupak, M. Eyal, D. Brusilovsky, R. Reisfeld, S. Graham and C. Klingshirn: *Appl. Phys. B.* **58**, 283 (1994).
- [226] L. T. Canham, *Appl. Phys. Lett.* **63**, 337 (1993).
- [227] A. Bruska, F. Cichos, F. Homilius, M. Hietschold and C. von Borczyskowski, *Photoluminescence of porous Silicon Doped with Coumarine 153*, *J. Lumin.* (submitted)
- [228] P. Gupta, V. L. Colvin, S. M. George: *Phys. Rev. B* **37**, 8274 (1988).
- [229] A. Takazawa, T. Tamura, M. Yamada: *Appl. Phys. Lett.* **63**, 940 (1993)
- [230] S. A. Bagnich, *Dynamics of Triplet Excitations of Aromatic Compounds in Porous Matrices*, submitted for publication in *Chem. Phys.*
- [231] L. L. Hech and J. K. West: *Chem. Rev.* **90**, 33 (1990)
- [232] P. Schuster, G. Zundel and C. Sandorfy, *The Hydrogen Bond. Recent Development in Theory and Experiments*, North-Holland Publishing Corp., Amsterdam-New York-Oxford, 1976, p. 60
- [233] V. I. Zemskii, I. K. Meshkovskii and I. A. Sokolov, *Optika i spektroskopiya* **59**, 328 (1985)
- [234] U. Even, K. Rademann, J. Jortner, N. Manor, R. Reisfeld: *Phys. Rev. Lett.* **52**, 2164 (1984)
- [235] F. Homilius, Ph. D work, private communications

- [236] M. Grundner, H. Jacob: Appl. Phys. A **39**, 73 (1986)
- [237] D. B. Wittry, D. F. Kyser: J. Appl. Phys **38**, 375 (1967).
- [238] Z. Yong-dong, J. Yi-xin, N. Yong-qiang: J. Lum. **60 & 61**, 404 (1994).
- [239] Ph. Dumas, M. Gu, C. Syrykh, A. Hallimaoui, F. Salvan, J. K. Gimzewski: J. Vac. Sci. Technol. B **12**, 2067 (1994)
- [240] M. Wilson, R. Ogden, D. B. Holt: J. Mater. Sci.**15**, 2321 (1980).
- [241] D. B. Holt, E. Napchan, L. Lazzarini, G. Salviati, M. Urchulutegui: Microscopy of Semiconducting Materials 1993, Proceedings of the Royal Microscopical Society Conference at Oxford University edited by A. G. Cullis, A. E. Staton-Bevan, J. L. Hutchison, (1993), 661
- [242] J. L. Batstone, M. A. Tischler, R. T. Collins: Proceedings of the L Annual Meeting of the Electron Microscopy Society of America, edited by G. W. Bailey, J. Bentley, J. A. Small, (San Francisco Press Inc., San Francisco, Cal.) 1992
- [243] A. Bruska, A. Chernook, S. Schulze, M. Hietschold, Appl. Phys. Lett. **68**, 2378 (1996)
- [244] Formation of the light-emitting patterns on porous silicon by electron beam; A. Bruska, U. Falke, St. Schulze, M. Hietschold; E-MRS 1996 Spring Meeting, June 4-7, 1996, Strasbourg, France, Thin Solid Films (submitted)
- [245] F. Grey: Adv. Mat. **5**, 704 (1993)
- [246] M. A. McCord, R. F. W. Pease: J. Vac. Sci. Technol. B **4**, 86 (1986)
- [247] V. V. Doa, M. J. Sailor: Appl. Phys. Lett. **60**, 619 (1992)

- [248] J. C. Barbour, D. Dimos, T. R. Guilinger, M. J. Kelly, S. S. Tsao: Appl. Phys. Lett. **59**, 2088 (1991)
- [249] A. J. Steck, J. Xu, H. C. Mogul, S. Morgren: Appl. Phys. Lett. **62**, 1982 (1993)
- [250] X. Bao, H. Yang, Appl. Phys. Lett. **63**, 2246 (1993)
- [251] P. Steiner, A. Richter, W. Lang: J. Micromech. Microeng. **3**, 32 (1993)
- [252] F. Müller, A.-D. Müller, M. Hietschold: Rev. Sci. Instrum. **66**, 4738 (1995)
- [253] Th. Pfeifer, Diplomarbeit "Herstellung und Untersuchung von Mikrostrukturen lumineszenten porösen Siliciums mit SXM-Methoden", TU Chemnitz 1996
- [254] B. Hacker, A. Hillebrand, T. Hartmann, R. Guckenberger: Ultramicroscopy **42-44**, 1514 (1992)
- [255] M. Röder, Diplomarbeit, TU Chemnitz 1993
- [256] C. E. Bach, R. J. Nichols, W. Beckmann, H. Meyer, A. Schulte, J. O. Besenhard, P. D. Jannakoudakis: J. Electrochem. Soc. **140**, 1281 (1993)

Selbständigkeitserklärung

Hiermit erkläre ich, daß ich die vorliegende Arbeit selbständig und nur unter Verwendung der im Literaturverzeichnis aufgeführten Quellen und Hilfsmittel angefertigt habe.

Anna Bruska

Chemnitz, den 19.09.1996

Thesen zur Dissertation

vorgelegt von Diplomphysikerin Anna Bruska

1. Nanoporöses Silizium (Si) hat in letzter Zeit starke internationale Aufmerksamkeit gefunden, da seine optoelektronischen Eigenschaften (Photo- und Elektrolumineszenz) möglicherweise eine integrierte Optoelektronik auf Si-Basis erlauben. Obwohl PS bereits seit über 30 Jahre bekannt ist, sind seine Lumineszenzeigenschaften noch nicht vollständig geklärt. Die Grundlage für eine optoelektronische Anwendung ist jedoch die Kontrollierbarkeit der Lumineszenzeigenschaften.

2. Ausgehend vom Kenntnisstand der PS Herstellung wurden die Ätzparameter bezüglich der Dotierung des Si Substrats, der Stromdichte, der HF-Konzentration, der Ätzzeit und einer eventuellen Nachbehandlung variiert. Es wurde reines, dotiertes und strukturiertes poröses Silizium untersucht. Zur Strukturcharakterisierung der Schichten wurden die Verfahren STM, SEM und TEM verwendet. PL, CL, PLE und zeitaufgelöste Spektroskopie wurden benutzt, um die optischen Eigenschaften von PS zu untersuchen.

3. Optische und Sekundärelektronenaufnahmen von freistehenden porösen Siliziumfilmen lassen die vorhergesagte Schichtstruktur erkennen. Der Ursprung dieses Effekts könnte in Inhomogenitäten im Ausgangsmaterial oder

in mechanischen Spannungen, die vom Ätzprozeß herrühren, liegen.

4. Es wurde eine Entwicklung der PL-Spektren von PS von einer Bande bei 1.88 eV zu zwei Banden bei 1.88 eV und bei 2.05 eV bei steigender Ätzstromdichte während der Herstellung gefunden. Im Gegensatz zur allgemeinen Deutung gehen wir nicht von einer Verschiebung der Bande aus, sondern von dem grundsätzlichen Vorhandensein zweier Banden, die je nach Wahl der Versuchsparameter selektiv verstärkt oder abgeschwächt werden.

5. Die einzelnen Lumineszenzbanden (bei 1.88 eV und bei 2.05 eV) lassen sich selektiv anregen, wobei die Peaklage unverändert bleibt. Dies läßt sich durch die Existenz von mindestens zwei Typen von Lumineszenzzentren erklären.

6. Die PL-Kurven wurden mit Hilfe einer Gaußauswertung (Summe von 2, 3 bzw. 4 Gußkurven) analysiert. Dabei haben wir gefunden, daß unsere Spektren generell gut durch eine Summe von zwei Gaußkurven bei 1.88 eV und 2.05 eV angepaßt werden können.

7. Ein Aufdampfen von Platin, das in der Elektronik neben Gold häufig als Kontaktschicht verwendet wird, führt zusätzlich zu einer Änderungen im Verhältnis beider Lumineszenzbanden bzw. erst zur deutlichen Herausbildung der Doppelpeakstruktur in der Lumineszenz.

8. Der erste Typ von Lumineszenzzentren (bei 2 eV) ist an der Oberfläche (Oxidschicht) lokalisiert, während der zweite Typ (bei 1.88 eV) mit tieferliegenden Störstellen (im Oxid bzw. an der Grenzfläche Oxid-Silizium) verbunden werden kann.

9. Nach einer Dotierung der PS-Proben mit einem Laserfarbstoff (Coumarine

153, Stilbene 1, Kiton Red and Rhodamine 110) haben wir eine Absenkung der Lumineszenzintensität sowie eine Verschiebung der Lumineszenzbande gefunden. Die niedrigere Intensität folgt aus der Absorption durch den Farbstoff. Die Verschiebung der Bande könnte die Folge einer Wechselwirkung des Farbstoffes mit den Lumineszenzzentren an der Oberfläche des PS sein.

10. Es ist möglich, mit Hilfe eines Elektronenstrahles ein optisches Muster im PS zu erzeugen. Diese Muster sind sowohl im Kathodolumineszenzbild im SEM als auch in der Photolumineszenz unter Anregung mit UV-Strahlung an Luft sichtbar.

11. Spektrale CL-Messungen an PS zeigen zwei Banden bei 2.7 eV und 2 eV. Es wurde gefunden, daß nach der Mustererzeugung jedoch nur noch die Bande bei 2.7 eV beobachtbar ist. Basierend auf unseren oben erwähnten Ergebnissen (dotierte und reine Proben) kann bestätigt werden, daß die Bande bei 2.0 eV von Störstellen in der Oberflächen(oxid)schicht hervorgerufen wird und diese im Fall der Bestrahlung mit einem Elektronenstrahl modifiziert oder zerstört wird. Die CL-Bande bei 2.7 eV stammt von tieferliegenden Störstellen im SiO_x , was mit in der Literatur zu findenden Ergebnissen übereinstimmt.

12. Mit Hilfe eines elektrochemischen Raster-Tunnel-Mikroskops ist es möglich, Mikrostrukturen porösen Siliziums herzustellen. Die gewonnenen Mikrostrukturen zeigen Kathodolumineszenz. Die poröse Struktur im Inneren des Ätzpunktes zeigt eine starke strukturelle Ähnlichkeit zu den herkömmlich gefertigten PS-Proben. Es kann eine enge Korrelation zwischen Ätzstrom und Strukturbildungsprozeß festgestellt werden.

13. Es konnte kein Einfluß des Ätzstromes auf den Durchmesser der Mikro-

strukturen gefunden werden. Dieser hängt vielmehr hauptsächlich von der Geometrie der Spitze und dem Abstand Probe-Spitze ab.

14. Eine genaue Abstandsregelung der Sondenspitze auf Basis eines potentiostatischen ECSTM-Konzepts würde eine Herstellung definierter und reproduzierbarer Mikrostrukturen ermöglichen, was eine Voraussetzung für mögliche technische Anwendungen ist.

Danksagung

Abschließend möchte ich allen denjenigen danken, die durch die angenehme Arbeitsatmosphäre und durch vielfältige Unterstützung zum Gelingen dieser Arbeit beigetragen haben:

Herrn Prof. Dr. rer. nat. habil. M. Hietschold für die hilfreiche, freundschaftliche Unterstützung und Betreuung meiner Doktorarbeit,

Herrn Prof. Dr. rer. nat. habil. Ch. von Borczyskowski für die Möglichkeit, die optischen Messungen in seinem Lehrstuhl durchführen zu können und für die wertvollen Diskussionen,

Herrn Prof. F. Richter für die Möglichkeit meine Arbeit im Rahmen des Graduiertenkollegs anzufertigen,

Herrn Dipl. Phys. U. Falke für die TEM-Aufnahmen des porösen Siliziums und Frau R. Zeugfang für ihre Hilfe bei der Arbeit am Rasterelektronenmikroskop,

Herrn Dipl. Phys. F. Cichos für die Messung der Lumineszenz-Zeitkonstanten und die liebevolle Unterstützung,

Herrn J. Lenzner für die spektralaufgelösten CL- Messungen,

Herrn Dipl. Phys. Th. Pfeifer für die experimentelle Mitarbeit an der Mikrostrukturierung von porösem Silizium mit SXM-Methoden,

Frau Dr. E.V. Astrova für die Präparation der PS-Proben ohne Substrat,

Herrn Dr. R. Wannemacher und Dr. P. Sitch für die Diskussionen und die Durchsicht des Manuskripts,

allen Kolleginnen und Kollegen am Lehrstuhl "Analytik an Festkörperoberflächen" für die angenehme, familiäre Atmosphäre und die fruchtbare Zusammenarbeit,

allen Mitarbeiter, die ich im Institut für Physik in Chemnitz kennenlernte für die freundliche Atmosphäre und Unterstützung während meiner Doktorarbeit. Ausdrücklich genannt seien: Dr. U. Rempel, Dr. M. Vogel, X. Grählert, A. Gruber, F. Homilius, Dr. O. Stenzel, Dr. H. Sbosny, A. Fechner, Dr. A. Tschernook,

sowie meiner Familie, besonders meiner Schwester, für Liebe und Vertrauen, ohne die nicht nur diese Arbeit nicht gelungen wäre.

Lebenslauf

Vorname : Anna
Name : Bruska
Geburtsdatum : 8 August 1969
Geburtsort : Torun, Polen
Familienstand: ledig

Bildung :

15.09.1993 - gegenwärtig	Technische Universität Chemnitz-Zwickau Institut für Physik, Professur : Analytik an Festkörperoberflächen, Promotionstudent (Graduiertenkolleg)
1.10.1988 - 26.08.1993	Nicholaus Copernicus Universität, Torun, Abschluß : Diplom-Physiker, Prädikat : sehr gut Thema der Diplomarbeit : Fotolumineszenz im ZnSe
1.10.1992 - 01.04.1993	Technische Universität Chemnitz-Zwickau, Praktikum im Labor, Professur : Analytik an Festkörperoberflächen Arbeit mit (Rastertunnel-, Rasterkraftmikroskopie)
1.02.1992 - 1.06.1992	College of Foreign Languages, Torun Kurs für Fortgeschrittene in amerikanischer Sprache
1.10.1984 - 30.06.1988	Nicholaus Copernicus Gymnasium, Torun

Berufliche Erfahrung :

1991 - 1.09.1993	Nicholaus Copernicus Universität, Torun Institut für Physik, Mikroelektroniklabor Wissenschaftlicher Assistent
------------------	--

Lehrtätigkeit :

02.1993 - 07.1993	Nicholaus Copernicus Universität, Torun, Institut für Physik, Mikroelektroniklabor, Praktikum für Physiker
02.1994 - 02.1995	Technische Universität Chemnitz-Zwickau, Physikalisches Praktikum für Physiker